

# REPORT DOCUMENTATION PAGE

AFRL-SR-BL-TR-01-

Public reporting burden for this collection of information is estimated to average 1 hour per response, including the gathering and maintaining the data needed, and completing and reviewing the collection of information. Send comments regarding this burden estimate or any other aspect of this collection of information, including suggestions for reducing this burden, to Washington Headquarters Services, Directorate for Information Operations and Reports, 1215 Jefferson Davis Highway, Suite 1204, Arlington, VA 22202-4302, and to the Office of Management and Budget, Paperwork Project Director, Washington, DC 20503.

0849

1. AGENCY USE ONLY (Leave blank)		2. REPORT DATE 10-OCT-01		3. REPORT TYPE AND DATES COVERED FINAL REPORT - 15 MARCH 99 TO 31 JULY 01	
4. TITLE AND SUBTITLE A COMMODITY SUPERCOMPUTER FOR TURBULENCE-CONTROL SIMULATIONS				5. FUNDING NUMBERS F49620-99-1-0184	
6. AUTHOR(S) JONATHAN B. FREUND					
7. PERFORMING ORGANIZATION NAME(S) AND ADDRESS(ES) THE REGENTS OF THE UNIVERSITY OF CALIFORNIA UNIVERSITY OF CALIFORNIA, LOS ANGELES 1401 UEBERROTH BLDG, BOX 951406 LOS ANGELES, CA 90095-1406				8. PERFORMING ORGANIZATION REPORT NUMBER	
9. SPONSORING/MONITORING AGENCY NAME(S) AND ADDRESS(ES) AFROS/NA 801 N. RANDOLPH STREET ROOM 732 ARLINGTON, VA 22203-1977				10. SPONSORING/MONITORING AGENCY REPORT NUMBER	
11. SUPPLEMENTARY NOTES				20011126 124	
12a. DISTRIBUTION AVAILABILITY STATEMENT  Approved for public release; distribution unlimited.				12b. DISTRIBUTION STATEMENT (AFOSR) NOTICE OF TRANSMITTAL DTIC. THIS TECHNICAL REPORT HAS BEEN REVIEWED AND IS APPROVED FOR PUBLIC RELEASE LAW AFR 190-12. DISTRIBUTION IS UNLIMITED.	
13. ABSTRACT (Maximum 200 words) Recent experiments have shown that properly designed high amplitude, low mass flux pulsed slot jets blowing normal to a jet's shear layer near the nozzle can significantly alter the jet's development (Parekh et al., AIAA Paper 96-0308). In contrast to commonly used low amplitude forcing, this strong excitation appears to overwhelm the turbulence, having nearly the same effect at high and low Reynolds numbers. It can therefore be studied in detail by numerical simulation. In this study, direct numerical simulations of Mach 0.9, Reynolds number 3600 jets exhausting into quiescent fluid are conducted. Physically realistic slot jet actuators are included in the simulation by adding localized body-"force" terms to the governing equations. Three cases are considered in detail: a baseline unforced case and two cases that are forced with flapping modes at Strouhal numbers 0.2 and 0.4 (St=0.4 was found to be the most amplified frequency in the unforced case). Forcing at either frequency causes that the jet to expand rapidly in the plane with the actuators and to contract in the plane perpendicular to the actuators, as observed experimentally. It is found that the jet responds closer to the nozzle when forced at St= 0.4, but forcing at =0.2 is more effective at spreading the jet further downstream. Several different measures of mixing (scalar dissipation, volume integrals of jet fluid mixture fraction, and point measurements of mixture fraction) are considered, and it is shown that by most, but not all, measures forcing at St = 0.2 is the more effective of the two at mixing.					
14. SUBJECT TERMS				15. NUMBER OF PAGES 64	
				16. PRICE CODE	
17. SECURITY CLASSIFICATION OF REPORT UNCLASSIFIED	18. SECURITY CLASSIFICATION OF THIS PAGE UNCLASSIFIED	19. SECURITY CLASSIFICATION OF ABSTRACT UNCLASSIFIED	20. LIMITATION OF ABSTRACT		

# FINAL REPORT: A COMMODITY SUPERCOMPUTER FOR TURBULENCE-CONTROL SIMULATIONS

DURIP Award #: F49620-99-1-0184

**Jonathan B. Freund and John Kim**  
Mechanical and Aerospace Engineering  
University of California, Los Angeles

The objective of this DURIP grant was to build a supercomputer out of commodity components to study turbulence and its control. This objective has been successfully met. This report summarizes the final configuration of the system that we built and documents the results of some simulations run on it, including some ongoing AFOSR sponsored work. The system continues to be used at a level near its capacity.

## Configuration

The final configuration of the system is as follows

Nodes	20 Compaq XP1000
Processors	Alpha EV6, 500 MHz
Memory	1×1 GB, 16×512 B, 3×256 MB
Disks	4 GB SCSI each node 50 GB SCSI
Network	Fast Ethernet Switch
Operating System	Linux (Red Hat)
Software	LAM MPI implementation Compaq Fortran
Mass Storage Unit 1	800 MHz Pentium 500 MB RAM 472 GB Disks (total)
Mass Storage Unit 2	2×1 GHz Pentium 1 GB RAM 472 GB Disks (total)

A comparison showed that after vendor discounts that the 20 XP1000's would, for the same price, offer comparable performance to Intel Pentiums and greater flexibility since single-processor jobs would run three times as fast. For many applications they are still faster than much newer 1.5GHz Pentium processors.

## Applications

The system has been used to provide computation support to AFOSR Grants

- Aeroacoustic Optimization and Control, Freund, 2000-2002

- Real-Time Feedback Control of Mixing in a Heated Jet, Freund (via subcontract), 1997-2000
- Development of Robust Boundary Layer Controllers, Kim, 1997-2000
- Robust Controllers for Turbulent Boundary Layers, Kim, 2000-2002

The following are copies of several publications resulting these projects. Detailed technical summaries will be/have been included in the final reports for the individual projects.

Summary of publications:

J. B. Freund & P. Moin, “Jet mixing enhancement by high amplitude fluidic actuation,” with P. Moin, *AIAA J.*, **38**(10), 1863–1870 (2000).

P. Koumoutsakos, J. B. Freund & D. Parekh, “Evolution strategies for automatic optimization of jet mixing,” *AIAA J.* **39**(5), 967–969 (2001).

M. Wei & J. B. Freund, “Optimal Control of Free Shear Flow Noise”, abstract accepted for the 40<sup>th</sup> Aerospace Sciences Meeting, Reno, Jan 14-17, 2002.

K. Lee, L. Cortelezzi, J. Kim & J. L. Speyer, “Application of reduced-order controller to turbulent flows for drag reduction,” *Phys. Fluids*, **13**(5), 2001.

# Jet mixing enhancement by high amplitude fluidic actuation

**Jonathan B. Freund**

*Department of Mechanical and Aerospace Engineering  
University of California, Los Angeles  
Los Angeles, California 90095  
Email: jfreund@seas.ucla.edu*

**Parviz Moin**

*Department of Mechanical Engineering  
Stanford University  
Stanford, California 94305*

## Abstract

Recent experiments have shown that properly designed high amplitude, low mass flux pulsed slot jets blowing normal to a jet's shear layer near the nozzle can significantly alter the jet's development (Parekh *et al.*, AIAA Paper 96-0308). In contrast to commonly used low amplitude forcing, this strong excitation appears to overwhelm the turbulence, having nearly the same effect at high and low Reynolds numbers. It can therefore be studied in detail by direct numerical simulation. In this study, direct numerical simulations of Mach 0.9, Reynolds number 3600 jets exhausting into quiescent fluid are conducted. Physically realistic slot jet actuators are included in the simulation by adding localized body-“force” terms to the governing equations. Three cases are considered in detail: a baseline unforced case and two cases that are forced with flapping modes at Strouhal numbers 0.2 and 0.4. ( $St = 0.4$  was found to be the most amplified frequency in the unforced case.) Forcing at either frequency causes the jet to expand rapidly in the plane parallel with the actuators and to contract in the plane perpendicular to the actuators, as observed experimentally. It is found that the jet responds closer to the nozzle when forced at  $St = 0.4$ , but forcing at  $St = 0.2$  is more effective at spreading the jet further downstream. Several different measures of mixing (scalar dissipation, volume integrals of jet fluid mixture fraction, and point measurements of mixture fraction) are considered, and it is shown that by most, but not all, measures forcing at  $St = 0.2$  is the more effective of the two at mixing.

## Nomenclature

$a$	= speed of sound
$D$	= jet diameter
$\mathcal{D}$	= planar integral of $ \nabla\xi $
$e$	= total energy
$\mathcal{J}$	= volume integral of $\xi^n$
$\mathcal{M}$	= planar integral of $\xi^n$
$r$	= radial coordinate
$r_o$	= jet nozzle radius
$St$	= forcing Strouhal number = $fD/U_j$
$T$	= temperature
$U_a$	= peak actuator fluid velocity
$U_j$	= jet exit velocity
$v_x$	= axial velocity
$v_r$	= radial velocity
$v_\theta$	= azimuthal velocity
$x$	= axial coordinate
$\theta$	= azimuthal coordinate
$\rho$	= fluid density
$\xi$	= jet fluid mixture fraction
$\omega$	= vorticity magnitude

## Introduction

There are several technological applications where enhanced jet mixing can lead to improved efficiency, reliability, or safety. For example, enhanced jet mixing can reduce temperatures on in-plume aerodynamic surfaces, such as the blown flap on a C-17 aircraft, and thus provide greater flexibility in the choice of materials for their construction. Similarly, the mixing efficiency of fuel jets in combustors is an important factor in their overall performance, with size and weight reductions possible if mixing is improved. In the present work we focus on free jets, with the principle objective being plume temperature reduction.

In general, attempts to control jets can be divided into two categories: active and passive. Examples of passive control are tabs located at the nozzle exit,<sup>1,2</sup> crown shaped nozzles,<sup>3</sup> and various other tailorings of the nozzle exit.<sup>4-6</sup> This list is far from exhaustive. Passive control is attractive because in many cases it entails only simple design modifications, a change in nozzle geometry for example. Also its simplicity typically makes the resulting hardware less subject to failure. However, active control, where nozzle conditions are continuously updated, has greater flexibility and therefore greater potential to modify the jet flow. In this study we analyze a recently proposed method for active control of high Reynolds number jets.<sup>7</sup>

In the past, active excitation has been used extensively to understand the dynamics of free shear flows, particularly the dynamics of the largest turbulent flow structures. Studies up to the mid 1980's are summarize by Ho & Huerre<sup>8</sup> and relatively more recent efforts are discussed by Koch *et al.*<sup>9</sup> and Ho *et al.*<sup>10</sup> Here, the excitation used was typically low amplitude, often serving only to seed instability waves in the flow in order to phase correlate coherent structures. Unfortunately, it seems that to modify the flow significantly at high Reynolds numbers, low amplitude forcing is ineffective because the applied perturbations are overwhelmed by the turbulence. Thus, control by low amplitude excitation is not practical in many flows of engineering interest.

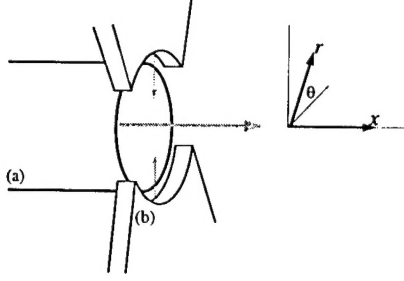


Figure 1: Geometry schematic showing the jet nozzle (a) and the actuators (b).

Recently, a scheme has been developed to control high Reynolds number jets, such as the exhaust flow from jet engines, by forcing with actuation velocities greater than the local turbulence intensity. This approach was tested by Parekh *et al.*<sup>7</sup> who designed slot jets that blew normal to the jet shear layer adjacent to the nozzle (as in figure 1). When pulsed 180° out of phase from one another with peak blowing at approximately one third the jet velocity (and approximately 2 percent of the jet mass flux), they excited large-scale oscillations in the jet that reduced the potential core length by over a factor of two. Recent test results have shown mixing enhancement using this technique on a full-scale engine.<sup>11</sup> Similar results have been obtained using zero net mass flux “synthetic jets”.<sup>7,12,13</sup> It appears that these active control approaches have been more successful at increasing mixing at high Reynolds numbers than any attempts by passive control approaches. Obviously the direct numerical simulations used in this effort are incapable of addressing high Reynolds number flows, but we shall see that the behavior of the simulated forced jets is similar to that observed at high Reynolds numbers, and new insights are provided.

Thus far, the forcing parameters in these experiments have been picked beforehand, as in an “open-loop” control strategy. “Closed-loop” control, where the jet flow would be continuously monitored and its state used to update the control parameters, may offer improved performance. To implement this approach a practical measure of the performance (an objective or “cost” function) is needed. An objective of the present effort is to study metrics for mixing and provide a database

for direct comparison of different metrics. The choice of a metric for a particular application will depend not only upon its relevance for the given mixing objective but also on practical aspects of its implementation. Here we concentrate only upon the metrics themselves.

## Flow parameters

The focus of this paper is a round jet at Mach 0.9. The jet Reynolds number, based upon centerline flow conditions at the nozzle exit, is 3600, and the stagnation temperature of the jet is constant. These parameters match those studied experimentally by Stromberg *et al.*<sup>14</sup> and a baseline, unforced case has been validated against their data.<sup>15</sup> Direct comparison shows that mean Mach number profiles (and the overall sound pressure levels on an arc at 60 radii from the nozzle) agree to within 5 percent. Unfortunately, the precise nozzle conditions were not measured, but spectra show that the initial jet shear layers were laminar, as expected at this Reynolds number. To model appropriate nozzle conditions a rounded ‘top-hat’ velocity profile was specified in the present simulations (see the Appendix). Small amplitude ( $v' < 0.01U_j$ ) random velocity fluctuations were added to this in order to seed the turbulence. The consequence of not adding random perturbations was a prolonged region of laminar flow near the nozzle, but the flow downstream was not particularly sensitive to the nature of these disturbances provided that they contained a range of frequencies and wavenumbers.

Slot jets pictured in figure 1 were used to excite the flow in a manner similar to the experiments of Parekh *et al.*<sup>7</sup> Each slot extended  $90^\circ$  around the jet and blew normal to the shear layers just downstream of the nozzle. The techniques for including these actuators in the simulations and their exact specifications are outlined with the numerical method in the Appendix. The individual slot jets blew  $180^\circ$  out of phase from one another to excite a flapping mode in the jet and their velocity varied sinusoidally between 0 and  $0.6U_j$ . The net mass-flow fraction of the actuators was  $\dot{M}_{act}/\dot{M}_{jet} \approx 0.035$ . Two forced jets were computed. The first was forced at Strouhal number

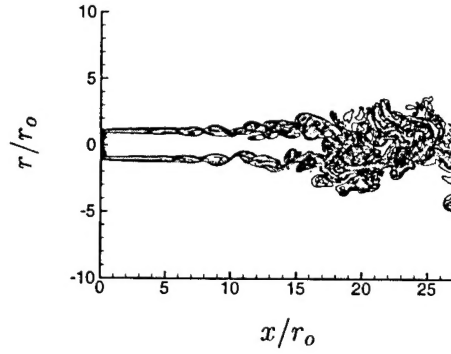


Figure 2: Vorticity magnitude contours for the unforced case in an  $x$ - $r$  plane. There are 40 evenly spaced contours with maximum  $\omega r_o/U_j = 8.43$ .

$St = 0.2$ , which had been found experimentally to be very effective at spreading the jet.<sup>7</sup> The other case was forced at  $St = 0.4$ , which was the most amplified frequency of the unforced jet, as found both by the simulations and the cited experiment.<sup>14</sup>

## Results

### Visualizations

Figure 2 shows a vorticity magnitude visualization of the unforced case. The initial jet shear layers are seen to be laminar. By  $x = 5r_o$  instability waves appear which develop into Kelvin-Helmholtz rollers by  $x = 10r_o$ . Their passing frequency is  $St = 0.4$ , in accord with the experiments of Stromberg *et al.*<sup>14</sup> who found that  $St = 0.44$  was the peak Strouhal number in the early development of their jet, subject to  $\pm 10\%$  day-to-day variation in their facility. At the instant shown the potential core extends to approximately  $x = 17r_o$ . Near the end of the potential core a transition to turbulence occurs which is corroborated by Reynolds stress statistics that will be reported elsewhere.<sup>15</sup>

Figure 3 shows a close-up of an actuator near its peak blowing condition. (The  $St = 0.2$  case is shown, but the  $St = 0.4$  case is similar.) There were only 8 mesh points across the modeled

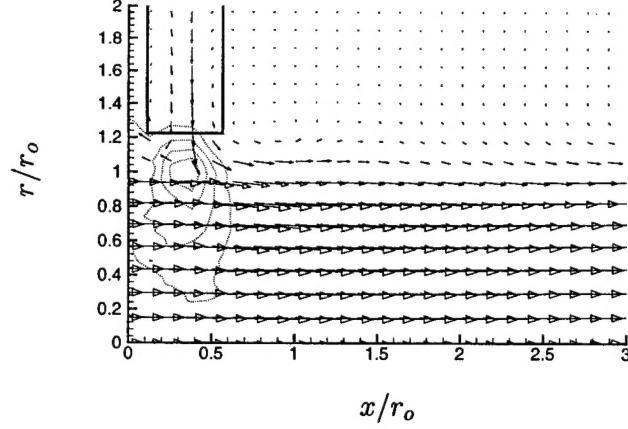


Figure 3: Actuator flow impinging on the jet shear layer. Every other mesh point in  $x$  and every sixth mesh point in  $r$  is shown. The solid rectangle indicated the extent of the actuator. Light contours show  $(p - p_\infty)/\rho_j U_j^2$  at evenly spaced intervals (min = 0.0333, max = 0.133).

actuator in the streamwise direction and those near the center of the actuator, where the Gaussian axial velocity distribution peaks (see the Appendix), carry most of the momentum flux. A region of increased pressure just below the actuator is also shown with contours in the figure. The initial effect of the forcing on the jet is seen just downstream of the actuator where the primary jet flow is slightly deflected. The bulk of the fluid exiting the actuator appears to be turned downstream as it encounters the jet, however a portion of it is also turned upstream, giving the appearance of a stagnation point flow. The pressure rise in this region is also reminiscent of a stagnation point flow.

The result of the forcing downstream is visualized in figures 4 and 5 for the  $St = 0.2$  and  $0.4$  cases respectively. It is clear for the  $St = 0.2$  case that the actuators excite the jet significantly and that it spreads rapidly in the  $\theta = \pi/2$  plane. In the  $\theta = 0$  plane, the spreading is suppressed. A single mode appears to dominate the early development of the jet as evidenced by the large structures visible before  $x = 10r_o$ . The instantaneous visualization in figure 4 shows the potential core closing at approximately  $x = 9r_o$ . Downstream of this region, the vorticity magnitude field shows an eruption of small-scale turbulence. A surprising feature of the visualization is the apparent

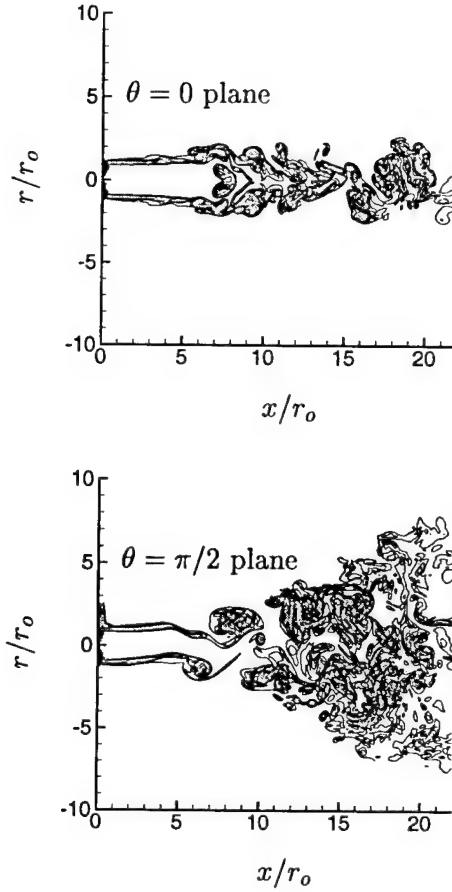


Figure 4: Vorticity magnitude contours for the cased forced at  $St = 0.2$ . Twenty evenly spaced contours between  $\omega r_o/U_j = 0.6$  and  $12.0$  are shown.

symmetry near  $x = 7r_o$  in the  $\theta = 0$  plane. This is the characteristic feature of the large-scale coherent structures seen in the  $\theta = \pi/2$  visualization as they intersect the  $\theta = 0$  plane.

When the jet is forced at  $St = 0.4$  (figure 5), the large-scale structures are smaller but appear earlier, which is not surprising because this is the most amplified frequency in the unforced jet. However, the downstream effect of the forcing is now quite different. The structures disappear or are obscured by small scales almost immediately and the jet spreads less in the plane of the actuators ( $\theta = \pi/2$ ). Though the shear layers appear thicker early in the development, they slow their spreading and merge only at around  $x = 13r_o$ , beyond where they merge in the  $St = 0.2$  case. The visualization in the  $\theta = 0$  plane is similar to the  $St = 0.2$  case, with similar symmetries at

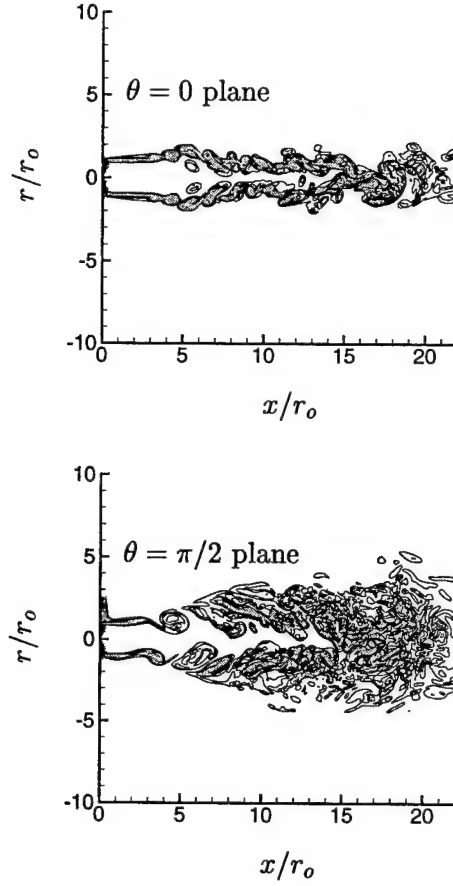


Figure 5: Vorticity magnitude contours for the case forced at  $St = 0.4$ . Twenty evenly spaced contours between  $\omega r_o/U_j = 0.6$  and  $12.0$  are shown.

small  $x$  due to the coherence of the excited structures, but a longer potential core.

Figure 6 shows a series of instantaneous visualizations of the jet fluid mixture fraction as it adjusts to forcing at  $St = 0.2$ . The time series starts from the unforced jet and the actuators turn on at  $t = 0$ . By  $t = 10r_o/U_j$ , there is clear evidence of large coherent structures distorting the scalar field. As expected, these travel at approximately  $0.65U_j$ , appearing at  $x \approx 10r_o$ , the horizontal midpoint of the region shown, at  $t \approx 15r_o/U_j$ . The scalar field takes considerably longer to develop further downstream where decreasing velocities slow advection. For computing statistics, the forced jets were assumed to be fully developed only after  $t = 80r_o/U_j$ . The simulations were run to approximately  $t = 150r_o/U_j$ .

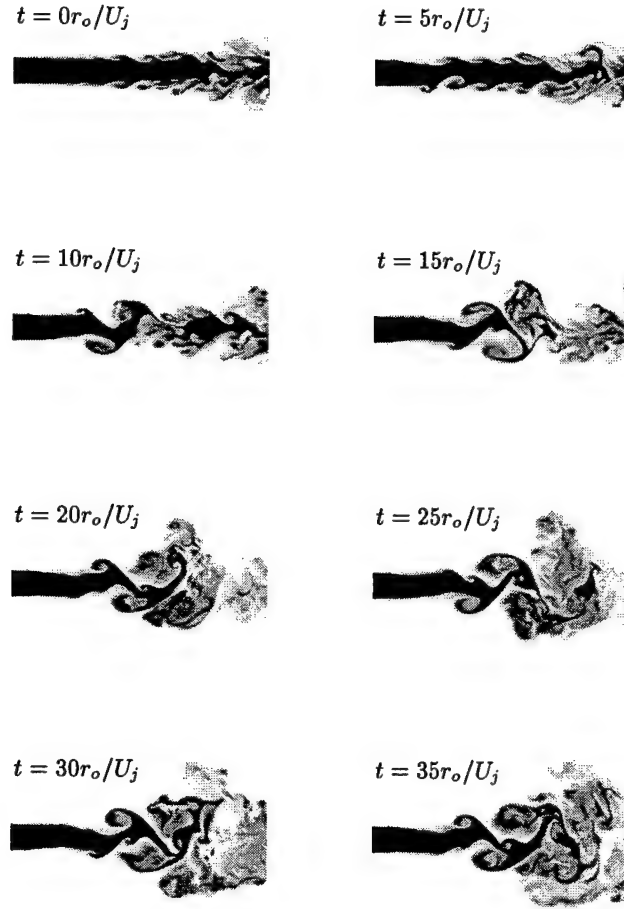


Figure 6: Development of the scalar field in the  $\theta = \pi/2$  plane once  $St = 0.2$  forcing is turned on at  $t = 0$ . Black is pure jet fluid, white is pure ambient fluid.

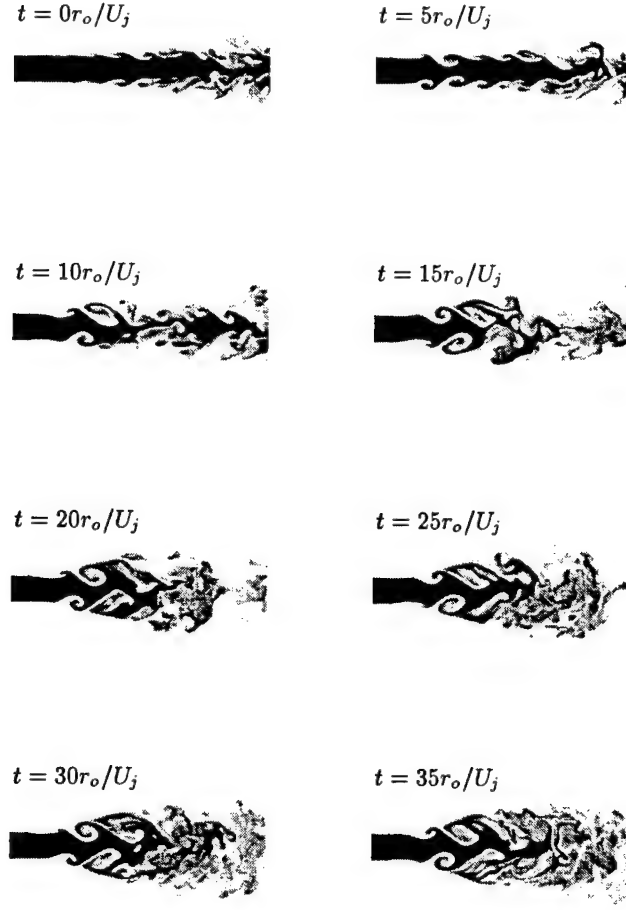


Figure 7: Development of the scalar field in the  $\theta = \pi/2$  plane once  $St = 0.4$  forcing is turned on at  $t = 0$ . Black is pure jet fluid, white is pure ambient fluid.

Figure 7 shows the corresponding set of images for the jet forced at  $St = 0.4$ . Again we see that at this forcing frequency, large structures appear closer to the nozzle than in the  $St = 0.2$  case. The mixed regions in the jet shear layers thicken rapidly, but a tongue of pure fluid persists along the domain centerline. The flapping of the jet column is also less pronounced.

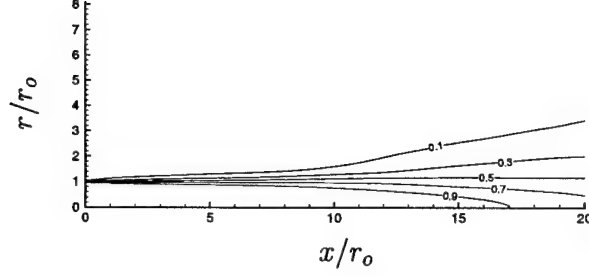


Figure 8: Mean axial velocity ( $\bar{v}_x/U_j$ ) for the unforced jet.

### Mean flow

Mean axial velocity ( $\bar{v}_x$ ) provides a more quantitative measure of the effect of the forcing on the jet development. Approximately 700 fields spaced in time by  $\Delta T_{\text{ave}} = 0.2r_o/U_j$  were averaged to compute the mean. Symmetries were exploited to increase the statistical sample. We see that the jet spreads as expected (see figure 8), first slowly where the shear layers are laminar, and then more quickly near the end of the potential core where the flow goes through transition. If  $\bar{v}_x/U_j = 0.9$  is used to designate the end of the potential core, in this case the potential core closes at  $x = 17r_o$ , which is further downstream than would be expected for high Reynolds number jets, because the shear layers are initially laminar and therefore spread slowly.

Forcing at  $St = 0.2$  dramatically alters the mean flow (figure 9). In the plane perpendicular to the action of the actuators ( $\theta = 0$ ) the jet at first spreads more rapidly than the unforced case, but then this is reversed starting at the end of the potential core ( $x = 8r_o$ ). Only near  $x = 20r_o$  does the 10 percent velocity contour extend to the same radial distance as at  $x = 8r_o$ . The contours have an unusual thumb shape at  $r = r_o$ ,  $x = 8r_o$  that is caused by the large-scale structures seen in figure 4. Based on visualizations (*e.g.* figure 4), these structures first intersect the  $\theta = 0$  plane near  $r = 0$ , and thus they bring lower velocity fluid into that region before the region near  $r = r_o$ . So at this downstream location the velocity is higher near  $r = r_o$  which causes the appearance of

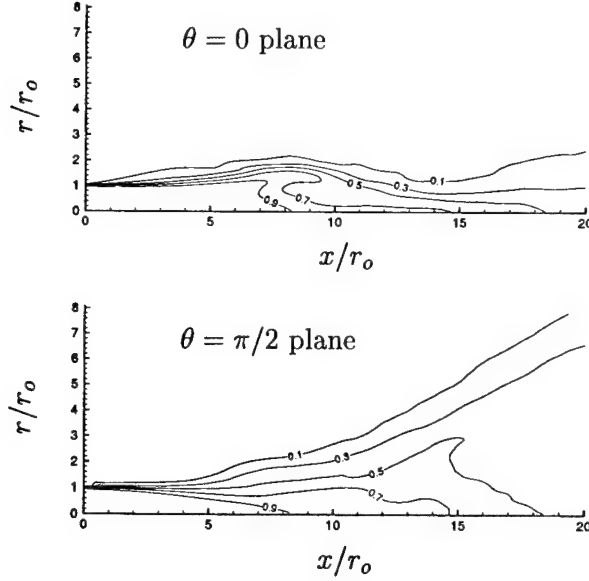


Figure 9: Mean axial velocity ( $\bar{v}_x/U_j$ ) for  $St = 0.2$  forcing.

the ‘thumb’. In the  $\theta = \pi/2$  plane, the jet is seen to spread rapidly starting near  $x = 8r_o$  and this continues until the end of the computational domain at  $x = 20r_o$ . Parekh *et al.*<sup>7</sup> showed very similar results for forcing at this same frequency.

When the jet is forced at  $St = 0.4$  (figure 10), the mean flow is markedly different. In the  $\theta = 0$  plane, the jet only spreads until around  $x = 5.5r_o$  before spreading is reversed. It does this significantly closer to the nozzle than in the  $St = 0.2$  case. There is again an unusual shape to the contours at this point, but at this forcing frequency it is less pronounced. Though spreading in the  $\theta = 0$  plane is reversed at smaller  $x$  than it was for  $St = 0.2$  forcing, the potential core is now longer, extending to  $x = 13.5r_o$ . In the  $\theta = \pi/2$  plane, the jet spreads rapidly starting at around  $5.5r_o$ , but spreading slows downstream and the jet does not grow as much radially as in the  $St = 0.2$  case (figure 9).

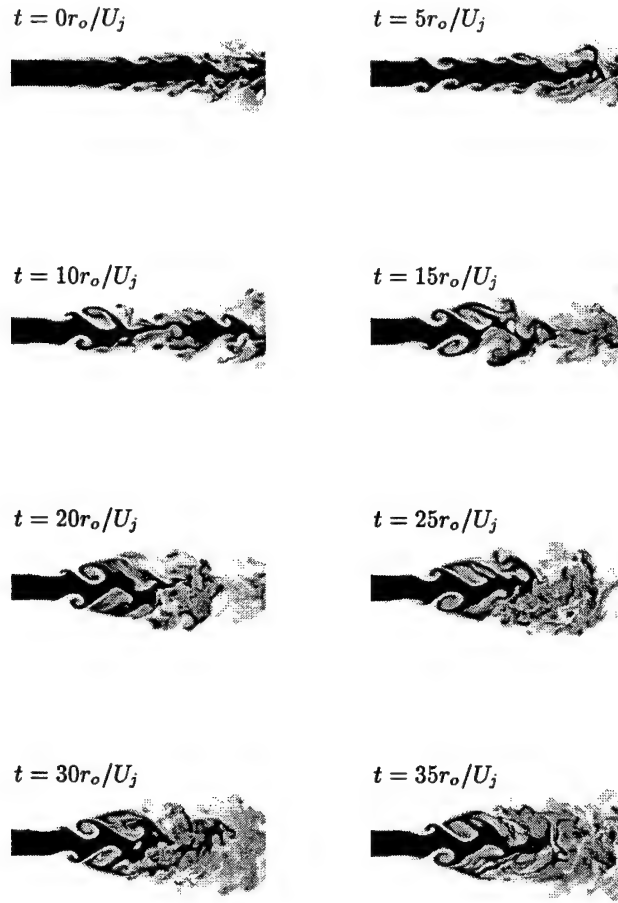


Figure 7: Development of the scalar field in the  $\theta = \pi/2$  plane once  $St = 0.4$  forcing is turned on at  $t = 0$ . Black is pure jet fluid, white is pure ambient fluid.

Figure 7 shows the corresponding set of images for the jet forced at  $St = 0.4$ . Again we see that at this forcing frequency, large structures appear closer to the nozzle than in the  $St = 0.2$  case. The mixed regions in the jet shear layers thicken rapidly, but a tongue of pure fluid persists along the domain centerline. The flapping of the jet column is also less pronounced.

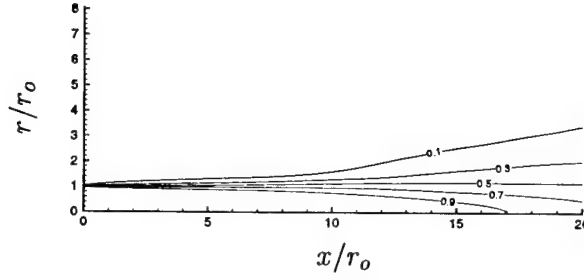


Figure 8: Mean axial velocity ( $\bar{v}_x/U_j$ ) for the unforced jet.

### Mean flow

Mean axial velocity ( $\bar{v}_x$ ) provides a more quantitative measure of the effect of the forcing on the jet development. Approximately 700 fields spaced in time by  $\Delta T_{\text{ave}} = 0.2r_o/U_j$  were averaged to compute the mean. Symmetries were exploited to increase the statistical sample. We see that the jet spreads as expected (see figure 8), first slowly where the shear layers are laminar, and then more quickly near the end of the potential core where the flow goes through transition. If  $\bar{v}_x/U_j = 0.9$  is used to designate the end of the potential core, in this case the potential core closes at  $x = 17r_o$ , which is further downstream than would be expected for high Reynolds number jets, because the shear layers are initially laminar and therefore spread slowly.

Forcing at  $St = 0.2$  dramatically alters the mean flow (figure 9). In the plane perpendicular to the action of the actuators ( $\theta = 0$ ) the jet at first spreads more rapidly than the unforced case, but then this is reversed starting at the end of the potential core ( $x = 8r_o$ ). Only near  $x = 20r_o$  does the 10 percent velocity contour extend to the same radial distance as at  $x = 8r_o$ . The contours have an unusual thumb shape at  $r = r_o$ ,  $x = 8r_o$  that is caused by the large-scale structures seen in figure 4. Based on visualizations (*e.g.* figure 4), these structures first intersect the  $\theta = 0$  plane near  $r = 0$ , and thus they bring lower velocity fluid into that region before the region near  $r = r_o$ . So at this downstream location the velocity is higher near  $r = r_o$  which causes the appearance of

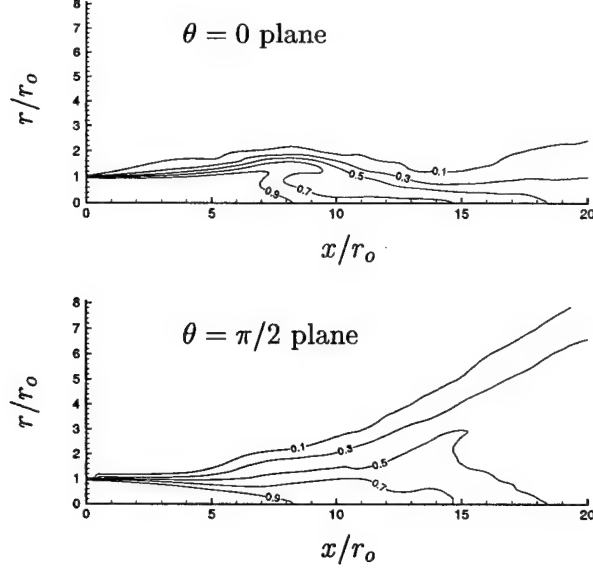


Figure 9: Mean axial velocity ( $\bar{v}_x/U_j$ ) for  $St = 0.2$  forcing.

the ‘thumb’. In the  $\theta = \pi/2$  plane, the jet is seen to spread rapidly starting near  $x = 8r_o$  and this continues until the end of the computational domain at  $x = 20r_o$ . Parekh *et al.*<sup>7</sup> showed very similar results for forcing at this same frequency.

When the jet is forced at  $St = 0.4$  (figure 10), the mean flow is markedly different. In the  $\theta = 0$  plane, the jet only spreads until around  $x = 5.5r_o$  before spreading is reversed. It does this significantly closer to the nozzle than in the  $St = 0.2$  case. There is again an unusual shape to the contours at this point, but at this forcing frequency it is less pronounced. Though spreading in the  $\theta = 0$  plane is reversed at smaller  $x$  than it was for  $St = 0.2$  forcing, the potential core is now longer, extending to  $x = 13.5r_o$ . In the  $\theta = \pi/2$  plane, the jet spreads rapidly starting at around  $5.5r_o$ , but spreading slows downstream and the jet does not grow as much radially as in the  $St = 0.2$  case (figure 9).

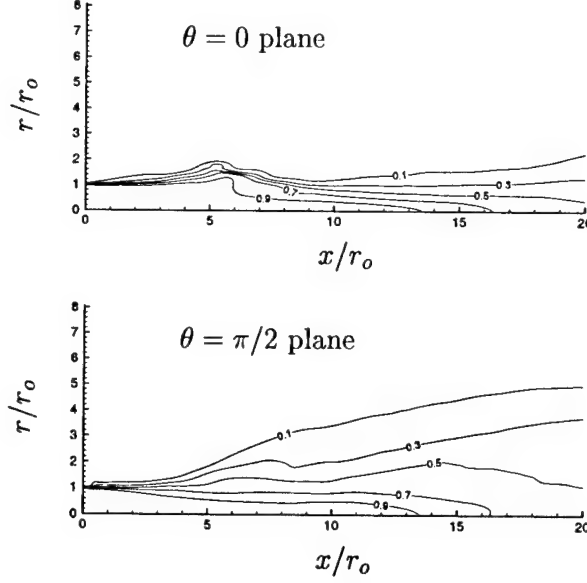


Figure 10: Mean axial velocity ( $\bar{v}_x/U_j$ ) for  $St = 0.4$  forcing.

### Unsteady response of the jet

To optimize the forcing, by either an open- or closed-loop approach, it is necessary to develop a measure of its effectiveness. Naturally, the choice of a definition for mixing effectiveness will depend upon the specific objective of the application. Here we will consider several metrics that are of potential use in temperature abatement or combustion applications.

#### *Point measurements of $\xi$*

We first consider point measures of jet fluid mixture fraction ( $\xi = 1$  for pure jet fluid and  $\xi = 0$  for pure ambient fluid) on the jet axis. If the jet were hot, the concentration of jet fluid (mixture fraction) would closely correspond to temperature. Extensive centerline measurements have been made in forced jets and have been used to estimate the mixing enhancement of various forcings.<sup>7</sup> Figure 11 shows time histories of  $\langle \xi \rangle$  on the jet axis ( $r = 0$ ) and at  $x = 5, 10, 15$  and  $20r_o$ . The angle braces  $\langle \rangle$  indicate an average over a single period of the forcing:  $T_a = 9.9r_o/U_j$  for  $St = 0.2$

and  $T_a = 4.9r_o/U_j$  for  $St = 0.4$ . Despite this average, there is still considerable oscillation in the measure due to the chaotic nature of turbulence. Averaging for longer periods would, of course, smooth the profiles, but for closed-loop control applications it is important to be able to quickly measure the response of the jet to changes in the forcing. Longer averages would slow the response of the metric to the changes in the forcing.

We see in figure 11 that before forcing is initiated at  $t = 0$ , the flow is pure jet fluid at  $x = 5r_o$  and  $x = 10r_o$ . At  $x = 15r_o$  there is slight mixing with ambient fluid and at  $x = 20$ , the mixture fraction hovers around its long-time (if forcing were not initiated) mean  $\bar{\xi} = 0.65$ . As expected from observations of the potential core length, the mixture fraction at  $x = 5r_o$  is unaffected by the forcing at either Strouhal number. At  $St = 0.2$  (figure 11 a), the mixture fraction at  $x = 10r_o$  is the first to respond to the forcing. It initially decreases to  $\langle \xi \rangle = 0.5$ , but rises again and remains near the mean  $\bar{\xi} = 0.75$  for  $t > 60r_o/U_j$ . The period averaged values at  $x = 15r_o$  and  $20r_o$  also seem to overshoot initially before they settle to hover around their apparent long-time mean values of  $\bar{\xi} = 0.6$  and  $\bar{\xi} = 0.3$  respectively. The small statistical sample size makes these values and the point where they are reached somewhat imprecise. Forcing at  $St = 0.4$  also causes a greater reduction in centerline mixture fraction initially (figure 11 b). The curve at  $x = 10r_o$  initially dips, but recovers to nearly its unforced, pure jet fluid level by  $t = 70r_o/U_j$ . The curves at  $x = 15r_o$  and  $20r_o$  hover around their mean values of  $\bar{\xi} = 0.7$  and  $\bar{\xi} = 0.4$ . It is unclear why this case takes longer to equilibrate than the lower frequency forcing.

The initial overreaction of the jet to the forcing can be explained qualitatively with a simple model where the large-scale structures are assumed to be linear instability waves. Given this model, turbulent structures will grow, stabilize, and decay as the layer spreads. If the jet spreads slowly, as in the unforced case, there is a long region of growth before decay. So, given a significant initial forcing amplitude, the structures can become quite intense by a linear mechanism. However, high

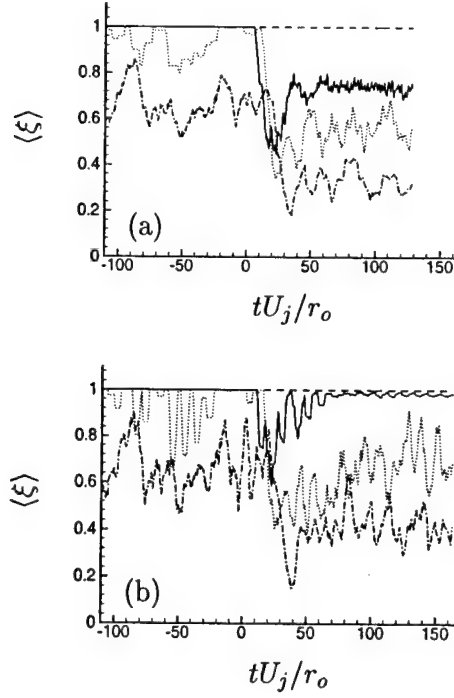


Figure 11: Time histories of scalar on the jet axis: ----  $x = 5r_o$ ; —  $x = 10r_o$ ; .....  $x = 15r_o$ ; and -·-·  $x = 20r_o$ . (a)  $St = 0.2$ ; (b)  $St = 0.4$ . Each curve shows a time average over one forcing period.

amplitude disturbances will also increase the spreading rate of the layer and thereby reduce the distance over which subsequent disturbances can amplify. Hence, by this model the first forced structure “sees” a slowly spreading layer and thus can grow more than subsequent disturbances that “see” a more rapidly spreading layer, which explains the observed overshoot.

This model can also explain the greater response of the jet to  $St = 0.2$  forcing than forcing at its natural frequency  $St = 0.4$ . Instability analysis shows that for thicker shear layers, as would be present in forced jets, the most amplified instability waves will have a longer wavelength and lower frequency.<sup>16</sup> Therefore, it is not surprising that  $St = 0.2$  is more successful. Unfortunately, linear stability predictions can only loosely model the quantitative behavior of turbulence. An accurate quantitative prediction using linear stability analysis is therefore not likely to be successful in conjunction with the high amplitude forcing used in the present study.

Volume integrals of  $\xi^n$  can also provide a measure of mixing effectiveness. For  $n \approx 4$  to 6 this will provide a crude model, assuming  $\xi \propto T$ , of the infrared signature of the jet. Time histories of

$$\mathcal{J} = \int_{\Omega_c} \xi^n dV, \quad (1)$$

where  $\Omega_c$  is the physical domain ( $x < 20r_o, r < 10r_o$ ), are shown in figure 12. No time averaging was necessary to smooth curves in this case. We see that the volume integrals of  $\xi^1$  and  $\xi^2$  both increase when the jet is forced. For both cases, the  $\xi^1$  curve shows that there is 60 percent more jet fluid in the domain. Despite this increase,  $\xi^4$  and  $\xi^6$  decrease thus indicating improved mixing. The  $\xi^6$  curve decreases from its unforced value  $\mathcal{J}_o$  to  $\mathcal{J} = 0.7\mathcal{J}_o$  for the  $St = 0.2$  case and  $\mathcal{J} = 0.6\mathcal{J}_o$  for the  $St = 0.4$  case. It is somewhat surprising that the  $St = 0.4$  case shows better mixing by this measure because the opposite was predicted based upon centerline measurements (figure 11). It may also seem counter to the visualizations and mean flow data which show greater spreading for  $St = 0.2$  forcing. Because (1) depends on the axial dimension of the computational box, it is therefore important to also estimate downstream mixing based upon the available data. (Note that the finite radial dimension does not affect the result because  $\xi \rightarrow 0$  by  $r = 10r_o$ , the radial box size.)

We can make such an extrapolation by computing mixedness as a function of downstream distance. Figure 13 shows the planar contributions to  $\mathcal{J}$  as a function of  $x$  for  $t > 80r_o/U_j$ :

$$\mathcal{M}_x(x) = \int_0^{2\pi} \int_0^{10r_o} \xi^6 r dr d\theta. \quad (2)$$

It now becomes clear that the apparent advantage of  $St = 0.4$  forcing is primarily a result of the

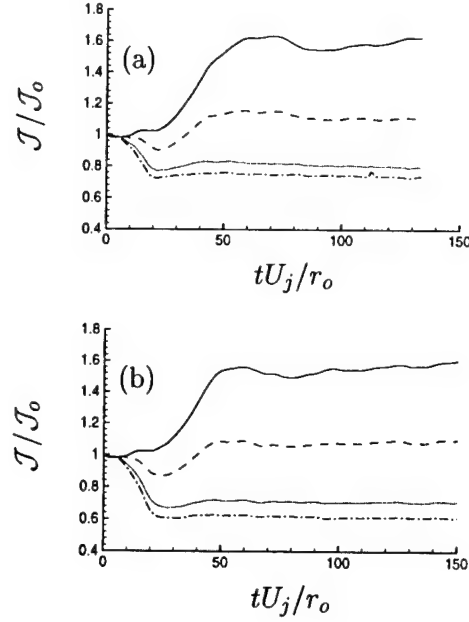


Figure 12: Integrals of  $\xi^n$  with  $n = 1$  — ;  $n = 2$  ---- ;  $n = 4$  ..... ;  $n = 6$  ——. (a)  $St = 0.2$  forcing; (b)  $St = 0.4$  forcing.

jet's more rapid response to the forcing. At the outflow boundary we see that the  $St = 0.2$  forced jet is actually mixed better (by this measure) and  $\mathcal{M}_x$  has a steeper slope (rate of mixing) than the jet forced at  $St = 0.4$ . Though it is not possible to make firm judgments about the subsequent downstream mixing, based on the level and slope of  $\mathcal{M}_x$  at  $x = 20r_o$  it appears that the  $St = 0.2$  case might be better if more downstream fluid could be included in (1). Both forced cases are clearly better than the unforced case also shown in the figure.

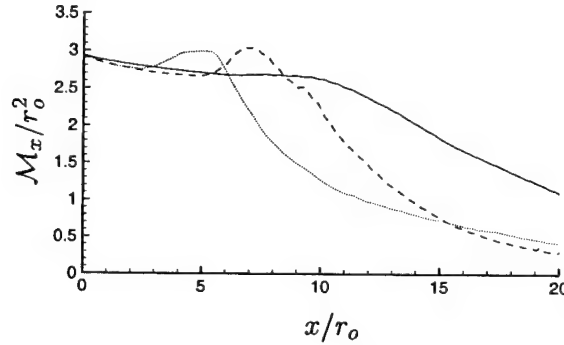


Figure 13: Planar integrals of  $\xi^6$  from (2): — unforced; ----  $St = 0.2$ ; .....  $St = 0.4$ .

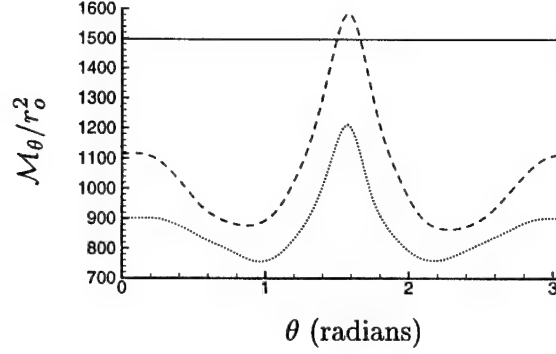


Figure 14: Planar integrals of  $\xi^6$  from (3): — unforced; ----  $St = 0.2$ ; .....  $St = 0.4$ .

The asymmetry of the jets is seen in figure 14 which shows planar integrals of  $\xi^6$  at constant  $\theta$ ,

$$\mathcal{M}_\theta(\theta) = \int_{-20r_o}^{20r_o} \int_0^{10r_o} \xi^6 dr dx. \quad (3)$$

For both forced cases, this metric peaks in the  $\theta = \pi/2$  plane, the plane of the actuators. For both Strouhal numbers, this peak is roughly 1.75 times as high as the minimum values. Somewhat surprisingly these minima do not occur at  $\theta = 0$  (see figure 14) which is perpendicular to the actuators.  $\mathcal{M}_\theta$  is 20 percent higher at  $\theta = 0$  than at its minima. Nearly everywhere  $\mathcal{M}_\theta$  is suppressed below its value in the unforced case, more so in the  $St = 0.4$  case. It should be noted that the details of these results also depend upon the box size. Because the forced jets are still highly asymmetric at the outflow boundary, the numerical differences between the peaks in valley would increase if more downstream data were available.

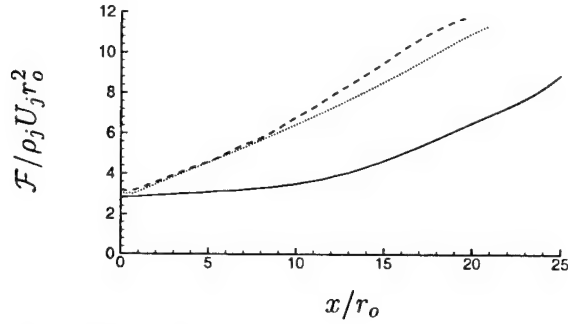


Figure 15: Streamwise mass flux from (4): — unforced; ----  $St = 0.2$ ; .....  $St = 0.4$ .

### *Streamwise mass flux*

The net entrainment of the jet can be studied by computing the streamwise mass flux. Because  $v_x$  is negligible at  $r = 10r_o$ , this is equivalent to

$$\mathcal{F}(x) = \int_0^{2\pi} \int_0^{10r_o} \overline{\rho v_x} r dr d\theta, \quad (4)$$

which is plotted in figure 15. The mass flux in the unforced case grows slowly at first, where the shear layers are laminar and disturbances are small, and then grows more rapidly starting at around  $x = 14r_o$  where the potential core closes. The mass fluxes in the forced cases both grow rapidly from the start and are over twice as high by  $x = 20r_o$ . Forcing at  $St = 0.2$  is only mildly more effective at increasing the mass flux than forcing at  $St = 0.4$ . It is seen that the fluxes are slightly different for the three cases at  $x = 0$ . This is because of the fluid added by the actuators and entrainment caused directly by their action.

### *Scalar dissipation*

The rate of scalar dissipation can also provide an important measure of mixing which is particularly relevant in combustion applications. In figure 16, we consider planar integrals of  $|\nabla \xi|$  as a function

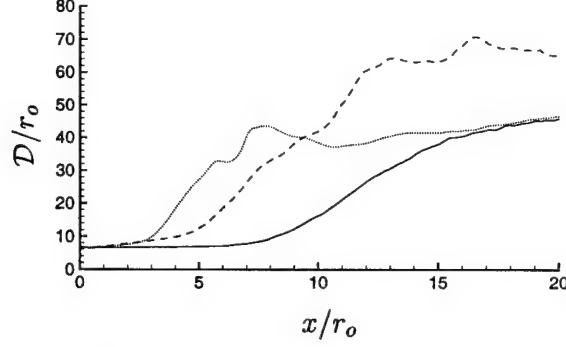


Figure 16: Planar integrals of  $|\nabla\xi|$  from (5): — unforced; ----  $St = 0.2$ ; .....  $St = 0.4$ .

of downstream distance,

$$\mathcal{D}(x) = \int_0^{2\pi} \int_0^{10r_o} |\nabla\xi| r dr d\theta. \quad (5)$$

$\mathcal{D}(x)$  for the  $St = 0.4$  case starts to rise closer to the nozzle, but the curve for  $St = 0.2$  forcing follows only  $2r_o$  further downstream and becomes 50 percent greater by the right side of the domain. The total dissipation in the computational domain is clearly larger for  $St = 0.2$  forcing. Based on the data at  $x = 20r_o$ , this trend is likely to continue downstream.

## Summary

Simulations of jets forced with high amplitude actuation reproduced experimental observations of similarly forced jets. Visualizations showed dramatic effect of this forcing on the jet. Forcing at  $St = 0.2$  excited the jet column into a distinct flapping mode. When forced at  $St = 0.4$ , the most amplified frequency in the unforced jet, the large structures appeared closer to the nozzle. However, despite the rapid initial spreading of this jet, forcing at  $St = 0.4$  was not as effective at spreading the jet and mixing it (by most measures) with the ambient flow downstream. Mean axial velocities showed that the jet becomes highly non-axisymmetric in both forced cases and that the potential

core length was reduced more by  $St = 0.2$  than  $St = 0.4$  forcing.

Mixing was quantified by several different metrics. Point measurements of scalar concentration on the jet axis showed that forcing at  $St = 0.2$  was more effective at reducing centerline scalar concentration. However, volume integrals of  $\xi^n$  over the computational domain (for  $n = 4$  or  $6$ ) were smaller when the jet was forced with  $St = 0.4$ . This was primarily due to the faster response of the jet to forcing at this frequency. Consideration of planar integrals of  $\xi^6$  and  $|\nabla\xi|$  as a function of  $x$  suggested that forcing at  $St = 0.2$  would be more effective for mixing further downstream. Forcing at both Strouhal numbers increased streamwise mass flux considerably over the unforced case, with  $St = 0.2$  forcing performing marginally better in this regard than  $St = 0.4$  forcing.

## Acknowledgements

The authors thank Dr. David Parekh and Dr. Alan Cain for many useful discussions on jet mixing, particularly with regard to the cited experimental studies. This work was supported by AFOSR.

## Appendix: Simulation techniques

The full compressible Navier-Stokes equations and an advection-diffusion equation were solved in cylindrical coordinates without modeling assumptions. Full details of the basic numerical algorithm are given by Freund *et al.*<sup>17</sup> where the same algorithm was used to study turbulence in compressible mixing layers. Only a summary of the method is provided here. Sixth-order compact finite differences<sup>18</sup> were used to compute derivatives in the streamwise ( $x$ ) and radial ( $r$ ) directions and Fourier spectral methods were used in the azimuthal direction ( $\theta$ ). A fourth-order Runge-Kutta algorithm was used to advance the solution in time. At the  $r = 0$  coordinate singularity, the equations were solved in Cartesian coordinates. To maintain a reasonable numerical time step given the

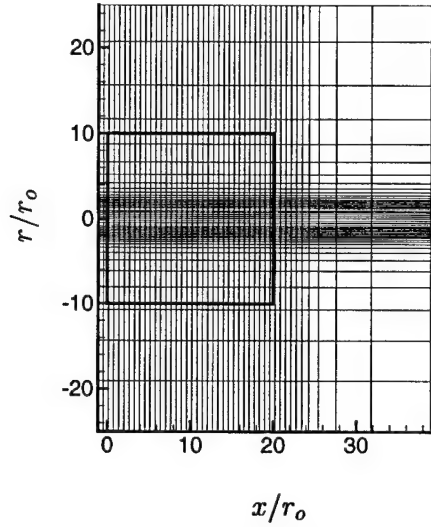


Figure 17: Mesh showing every tenth mesh point for the forced jet simulations. The thick rectangle demarks the physical portion of the computational domain.

restriction imposed by the Runge-Kutta algorithm, higher Fourier modes in  $\theta$  were not used near  $r = 0$ . They were omitted systematically so that the effective azimuthal resolution remained nearly constant with radial location. The computational mesh had  $440 \times 230 \times 160$  points in the axial, radial, and azimuthal directions respectively. Mesh points were compressed in the radial direction around  $r = r_o$ .

The boundary conditions, the jet nozzle, and the actuators were all accounted for by modifying the equations in appropriate regions of the computational domain. The rest of the computational domain that is free of these terms is referred to as the “physical domain”. The artificial terms serve to model an infinite domain, the nozzle, or the actuators where needed. For example, non-reflecting outflow and lateral (large  $r$ ) boundary conditions were approximated by stretching the mesh beyond the physical domain and filtering the solution on that stretched mesh. A typical mesh is shown in figure 17. Similar boundary conditions have been used in aeroacoustic computations and additional documentation is available elsewhere.<sup>15,19</sup>

In a zone of width  $r_o$  at the inflow side of the computational domain (see figure 17), terms

were added to the equations that drive the solution toward the desired nozzle conditions. If the compressible flow equations are represented by  $N(\mathbf{q}) = 0$ , where  $\mathbf{q}$  is a vector of flow quantities, then the modified equation has the form  $N(\mathbf{q}) = -\sigma(\mathbf{q} - \mathbf{q}_{\text{target}})$ , where  $\mathbf{q}_{\text{target}}$  is the desired nozzle conditions. The added term acts like a penalty function. The value of  $\sigma$  in this zone was  $2.5a_\infty/r_o$  and the target axial velocity was a typical hyperbolic tangent ‘top-hat’ profile:

$$\frac{\bar{v}_{x_{\text{target}}}}{U_j} = \frac{1}{2} \left[ 1 - \tanh \left[ 12.5 \left( \frac{r}{r_o} - \frac{r_o}{r} \right) \right] \right]. \quad (6)$$

The density and scalar profiles were similarly specified. Random velocity fluctuations were added to this mean profile using a similar body-“force” method. This randomization was low amplitude ( $v' < 0.01U_j$ ) and served only to seed the turbulence with broad-banded noise.

The actuators were included by similar body-force methods. The actuators extended axially from  $x_1 = 0.13r_o$  to  $x_2 = 0.57r_o$  (8 mesh points) and radially from  $r_1 = 1.11r_o$  to  $r_2 = 3.5r_o$  (101 mesh points). In this region,  $\sigma = 2.5a_\infty/r_o$  and  $\mathbf{q}_{\text{target}} = [\rho, \rho v_x, \rho v_r, \rho v_\theta, e, \rho \xi]_{\text{target}}^T = [.75\rho_\infty, 0, -.75\rho_\infty v_a, 0, e_a, 0]^T$  with  $e_a$  calculated from  $\rho = .75\rho_\infty$ ,  $v_a$ , and the ambient pressure. The instantaneous actuator target velocity was

$$v_a = U_a f_x(x) f_r(r) f_\theta(\theta) f_t(t). \quad (7)$$

Its amplitude was set at  $U_a = U_j$ , but the actual peak  $v_r$  at the actuator only reached  $0.6U_j$  because

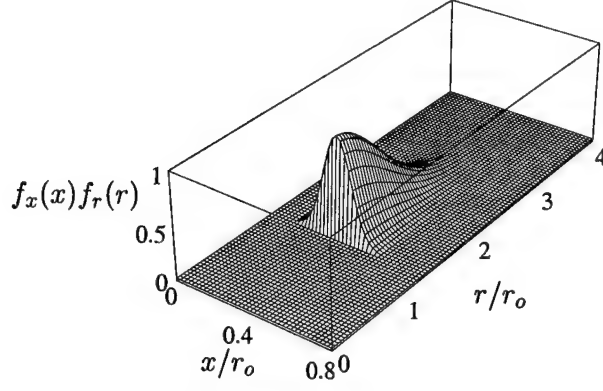


Figure 18: The  $x$ - $r$  shape of the actuation velocity.

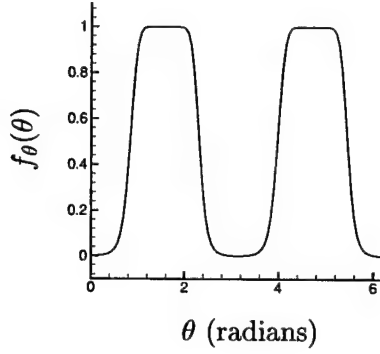


Figure 19: The  $\theta$  shape of the actuation velocity.

the body forcing was resisted by viscosity. The spatial and temporal dependencies of  $v_a$  were

$$f_x(x) = e^{-\alpha_x(x-0.5(x_1+x_2))^2} \quad (8)$$

$$f_r(r) = e^{-\alpha_r(r-r_1)^2} \quad (9)$$

$$f_\theta(\theta) = \exp[-\zeta(\theta)^{8e^{-\zeta(\theta)^2}+2.8}] + \exp[-(\zeta(\theta)-4)^{8e^{-(\zeta(\theta)-4)^2}+2.8}] \quad (10)$$

$$f_t(t) = 0.5[1 + \sin(2\pi St U_j t/D) \text{sgn}(\sin \theta)], \quad (11)$$

where  $\alpha_x = 95.1$ ,  $\alpha_r = 1.34$ , and  $\zeta(\theta) = 8\theta/2\pi - 2$ . The  $x$ - $r$  shape of  $v_a$  is plotted in figure 18 and the azimuthal dependence is plotted in figure 19. The ‘sgn’ term in (11) makes the actuators act out of phase.

## References

- [1] M. Samimy, K. B. M. Q. Zaman and M. F. Reeder, "Effect of tabs on the flow and noise field of an axisymmetric jet," *AIAA J.* **31**, 609 (1993).
- [2] M. F. Reeder and M. Samimy, "The evolution of a jet with vortex generating tabs: real-time visualization and quantitative measurements," *J. Fluid Mech.* **311**, 73 (1996).
- [3] E. K. Longmire, J. K. Eaton and C. J. Elkins, "Control of jet structure by crown-shaped nozzles," *AIAA J.* **30**, 505 (1992).
- [4] R. W. Wlezien and V. Kibens, "Influence of nozzle asymmetry on supersonic jets," *AIAA J.* **26**, 27 (1988).
- [5] A. Krothapalli, J. McDaniel and D. Baganoff, "Effect of slotting on the noise of an axisymmetric supersonic jet," *AIAA J.* **28**, 2136 (1990).
- [6] K. M. B. Q. Zaman, "Spreading characteristics of compressible jets from nozzles of various geometries," *J. Fluid Mech.* **383**, 197 (March 1999).
- [7] D. E. Parekh, V. Kibens, A. Glezer, J. M. Wiltse and D. M. Smith, "Innovative jet flow control: mixing enhancement experiments," *AIAA Paper 96-0308* (1996).
- [8] C.-M. Ho and P. Huerre, "Perturbed free shear layers," *Ann. Rev. Fluid Mech.* **16**, 365 (1984).
- [9] C. R. Koch, M. G. Mungal, W. C. Reynolds and J. D. Powell, "Helical modes in an acoustically excited round jet," *Phys. Fluids A* **1**, 1429 (1989).
- [10] C.-M. Ho, Y. Zohar, J. K. Foss and J. C. Buell, "Phase decorrelation of coherent structures in a free shear layer," *J. Fluid Mech.* **230**, 319 (1991).

- [11] G. McKinney, Air Force Office of Scientific Research Publication: Research Highlights, Sept./Oct 1998 (also <http://ecs.rams.com/afosr/afr/afo/any/text/any/afrrhoct.htm>).
- [12] B. L. Smith and A. Glezer, "The formation and evolution of synthetic jets," *Phys. Fluids* **10**, 2281 (1998).
- [13] B. L. Smith and A. Glezer, "Vectoring and small-scale motions effected in free shear flows using synthetic jet actuators," AIAA Paper 97-0213 (1997).
- [14] J. L. Stromberg, D. K. McLaughlin and T. R. Troutt, "Flow field and acoustic properties of a Mach number 0.9 jet at a low Reynolds number," *J. of Sound and Vib.* **72**, 159 (1980).
- [15] J. B. Freund, "Noise sources in a low Reynolds number turbulent jet at Mach 0.9," submitted *J. Fluid Mech.* (1999).
- [16] A. Michalke, "A survey on jet instability theory," *Progress in Aerospace Sciences* **21**, 159 (1984).
- [17] J. B. Freund, P. Moin and S. K. Lele, "Compressibility effects in a turbulent annular mixing layer," Technical Report TF-72, Stanford University, Mechanical Engineering, Flow Physics and Computation Division (1997).
- [18] S. K. Lele, "Compact finite difference schemes with spectral-like resolution," *J. Comp. Phys.* **103**, 16 (1992).
- [19] T. Colonius, S. K. Lele and P. Moin, "Boundary conditions for direct computation of aerodynamic sound generation," *AIAA J.* **31**, 1174 (1993).

# EVOLUTION STRATEGIES FOR AUTOMATIC OPTIMIZATION OF JET MIXING

**Petros Koumoutsakos**

Institute of Computational Sciences  
Swiss Federal Institute of Technology  
Zurich, CH-8092, Switzerland  
petros@inf.ethz.ch

**Jonathan Freund**

Mechanical and Aerospace Engineering  
University of California, Los Angeles  
Los Angeles, California  
jfreund@ucla.edu

**David Parekh**

Georgia Tech Research Institute  
Atlanta, Georgia  
david.parekh@gtri.gatech.edu

# 1 Introduction

Evolution strategies (ES) are introduced for the optimization of active control parameters for enhancing jet mixing. It is shown that the evolution algorithms can identify, in an automated fashion, not only previously known effective actuations but also find good but previously unidentified parameters. In this study simulations of model jets are used to demonstrate the feasibility of the methods. Evolution strategies are robust, highly parallel and portable algorithms that may be most useful in an experimental setting at realistic Reynolds numbers. Simulations of inviscid incompressible flows using vortex models as well as direct numerical simulations (DNS) of very low Reynolds number compressible flows are used in this study to evaluate different forcing parameters.

Our objective is twofold: (i) explore the possibility of ES to find previously identified modes of efficient operation, and (ii) discover previously unknown effective actuations. Practical engineering concerns will dictate the choice of actuator parameters and relevant cost functions. In Section 2 we present a description of the ES; in Section 3 we present results from the application of these to the optimization of compressible jets and vortex models. Section 4 is a discussion of results and an outline for future research.

## 2 Evolution Strategies

Evolution strategies are continuous parameter optimization techniques based on principles of evolution such as reproduction, mutation and selection. We define a vector in the control parameter space  $\vec{x} = (x_1, x_2, \dots, x_M)$  as an *individual* and a set of such individuals as a *population*. Evolution strategies use a *fitness value*, prescribed by  $F(\vec{x}) = F(x_1, x_2, \dots, x_M)$ , to identify the best individual from a population. We take better individuals to have larger  $F$  values.

### 2.1 Two-membered Evolution Strategies

The simplest evolution strategy has a population with two competing individuals, a *two-membered strategy*. Evolution occurs by *mutation* and *selection*, the two operations that Darwin considered

the most important in the evolution of species. Each individual is represented by a pair of real vectors  $\vec{u} = \vec{u}(\vec{x}, \vec{\sigma})$ , where  $\vec{\sigma}$  is an  $M$ -dimensional vector of standard deviations.

Following Rechenberg,<sup>1</sup> the optimization algorithm is as follows:

1. *Initialization*: A parent genotype consisting of  $M$ -genes is specified initially as  $\vec{x}^0$ .
2. *Mutation*: The parent of generation- $n$  produces a descendant with slightly different genotype. The operation of mutation is realized by modifying  $\vec{x}_p$  according to  $\vec{x}_c^n = \vec{x}_p^n + \vec{\mathcal{N}}(\vec{\sigma}_p^n)$ , where  $\mathcal{N}(\vec{\sigma})$  denotes an  $M$ -dimensional vector of normal random number with zero mean and standard deviations  $\vec{\sigma}$ .
3. *Selection*: The fittest individual according to its  $F$  value becomes the parent of the next generation:

$$\vec{x}_p^{n+1} = \begin{cases} \vec{x}_p^n, & \text{if } F(\vec{x}_p^n) \geq F(\vec{x}_c^n); \\ \vec{x}_c^n, & \text{otherwise.} \end{cases} \quad (1)$$

The variance of the population members is adjusted using the *1/5 success rule* proposed by Rechenberg: if more than one in five offsprings result in an improved solution, then the variance is increased.<sup>1</sup> For *regular optimization problems*<sup>2</sup> the method is known to converge to a global minimum, but the rate of convergence cannot be anticipated. So in finite time there is, of course, no guarantee that the global optimum has been reached, a trait shared by all optimization techniques. Schwefel<sup>3</sup> provides a complete description of the algorithm.

## 2.2 Parameter constraints

In problems of active flow control, engineering considerations impose constraints on the actuation parameters. Such constraints are formulated as inequalities, such as  $C_j(\vec{x}) \geq 0$ . In this work descendants that do not satisfy the constraints are treated as unsuccessful mutations.

### 3 Jet Flows Optimization

#### 3.1 Optimized Excitation of Compressible Jets

Direct numerical simulations of the developing region of compressible jets forced by slot-jet fluidic actuators are used to evaluate the fitness of individuals. The compressible flow equations were solved directly using a combination of sixth-order compact finite differences, spectral methods, and fourth-order Runge-Kutta time advancement. Further details of the numerical algorithm and techniques for including two slot-jet actuators that each span  $90^\circ$  of the jet (on opposite sides) just downstream of the nozzle were reported elsewhere.<sup>4</sup> Despite the low Reynolds number dictated by the computational expense (only  $Re = 500$  in this study) the actuators were able to induce the gross effects observed in experiments at much higher Reynolds numbers.<sup>5</sup> A path to implementation at more relevant flow conditions is discussed in Section 4.

For this study, only three actuation parameters were varied: the amplitude, frequency, and phase. The actuation is taken as a sum of harmonic waveforms:

$$v_r = \text{MAX} \left( \sum_{i=1}^N A_i \left[ 1 + \sin \left( U_j \frac{St_i}{D} t + \phi_i \right) \text{sgn}[\cos \theta] \right], \frac{U_j}{2} \right), \quad (2)$$

where  $v_r$  is the radial velocity at the actuator exit,  $U_j$  is the jet exit velocity,  $A_i$  are the amplitudes,  $St_i$  are the Strouhal numbers, and  $\phi_i$  are the phases of the different modes. The  $\text{sgn}[\cos(\theta)]$  factor causes each waveform to excite a flapping mode in the jet. Note that the phases,  $\phi_i$ , are the relative phases of the different modes—the two actuators always acted  $180^\circ$  out of phase. The  $A_i$  were constrained to be non-negative and the  $St_i$  were restricted to be  $0 \leq St \leq 0.8$ . The relative phases were not constrained.

The computational mesh was  $112 \times 42 \times 16$  in the streamwise, radial, and azimuthal direction respectively and the computational domain extended to  $16r_o$  downstream and  $5r_o$  in the radial direction, where  $r_o$  is the jet radius. A stretched-mesh boundary zone was positioned in  $x > 8r_o$  and  $r > 3.5r_o$  to absorb out-flowing fluctuations.<sup>4</sup> In each iteration of the optimization the jet was

simulated starting from an unforced case for several periods of forcing after the passing of initial transients. Because the flow is laminar and becomes quasi-periodic, this was sufficient to provide a measure of the long-time actuator effectiveness. In total 200 iteration were made.

Three wave forms ( $N = 3$ ) were used. The initial parameters and the parameters that maximized  $F$  are shown in Table 1. The fitness function was defined as

$$F = \int_{4r_o}^{8r_o} \int_0^{2\pi} \int_0^{3.5r_o} v_r^2 r dr d\theta dx, \quad (3)$$

which was evaluated using a trapezoidal rule quadrature and increased by a factor of 10 for the best parameters.

INITIAL			BEST		
$A_i/U$	$St_i$	$\phi_i$	$A_i/U$	$St_i$	$\phi_i$
0.45	0.50	0.00	0.04	0.33	0.54
0.40	0.20	0.70	0.42	0.17	0.31
0.35	0.50	1.00	0.07	0.45	1.57

Table 1: Initial and best actuation parameters.

It is interesting to note that the evolution strategy reduced the amplitude of two of the wave modes to a very low level giving effectively the same excitation that was shown to be successful in experiments<sup>5</sup> and in higher Reynolds number simulations on larger meshes.<sup>4</sup> This also demonstrates the mesh independence of the computation and its accuracy, at least for this measure of mixing. Notice also that the maximum amplitude stayed below half the jet velocity indicating that a sinusoidal profile was preferable to one that was clipped by the maximum amplitude constraint in (2). Scalar mixture fraction is visualized in figure 1 for the initial and best cases. The best case clearly shows high-amplitude flapping.

### 3.2 Incompressible Vortex Model

In these simulations it is assumed that the effects of compressibility and viscosity do not affect the flow dynamics and the circular jet is modeled by the combination of discrete vortex filaments and a fixed semi-infinite cylindrical sheet of vorticity with circulation per unit length  $\gamma$  that represents the

nozzle. Helical excitation as used in the experiments of Lee & Reynolds<sup>6</sup> is modeled by rotating the axis of the vortex cylinder with displacement  $A_h/r_o$  about the nominal jet centerline. The rotation frequency is denoted by  $f_h$  and the axial frequency is defined as  $f_a = St_a\gamma/2r_o$ . The frequency  $f_a$  is the rate at which filaments are generated at the origin. The velocities induced by each filament and the vortex sheet are added to determine the trajectory of each filament.  $St_a$  sets the time between creation of new rings. The circulation of each shed filament is  $\gamma = St_a\Gamma/R$ .  $\beta$  fixes the ratio of the axial to orbital excitation, and  $\phi$  sets their relative phase. Further details of this model and its numerical implementation were reported by Parekh *et al.*,<sup>7</sup> which also provided a detailed validation of the method through direct comparison with bifurcating jet experiments and refinements of the vortex ring representations.<sup>6</sup>

The control parameters were constrained so that  $0 \leq A_h \leq 1$ ,  $0.1 \leq St_a \leq 1$ ,  $0.2 \leq \beta \leq 5$ ,  $0 \leq \phi \leq 2\pi$ . The fitness function was the average angle of the ring trajectories defined as the angle between the jet centerline and the line that connects the center of the jet exit to the centroid of the vortex ring nodes. This metric was evaluated after eleven periods of axial excitation.

Initially we expected the algorithm to select a jet that bifurcates in a single plane with values of  $St_a$  and  $A_h$  that maximize the spreading angle as seen in laboratory jets.<sup>6</sup> Instead, a jet flow was found that had never been observed in previous experiments or calculations. It initially resembles a bifurcating jet (Fig. 2), but several diameters downstream the two branches of the jet exhibit a secondary bifurcation in which the rings change direction by about  $45^\circ$ . This results in a wide spreading angle as seen in Fig. 2. Unfortunately, the parameters that lead to this double bifurcation have not been tested experimentally so the code can not be validated for this case as is was for the other cases.<sup>7</sup> Regardless, the possibility that ES can identify novel control parameters has been demonstrated.

## 4 Summary and Conclusions

Given the variety of different forcing schemes, cost functions, and flows to be controlled, it is impossible to anticipate the best optimization scheme for any particular case, but the present

results clearly demonstrate that ES can be a valuable tool for jet mixing optimization. They identified, in an automated fashion, previously known flow controls and found previously unknown parameters that further enhance spreading. Their strength is their portability, which is considered particularly attractive for problems such as jet noise control flow where the mechanisms appear too poorly understood to provide much direct guidance.

In computational studies, such as the present, finite computational resources restrict the Reynolds numbers that can be addressed. The implementation of turbulence models and large-eddy simulation calculations is a natural next step, and is being carried out.<sup>8</sup> Besides computations, experiments are appealing for many applications as they can provide rapid answers at realistic flow conditions. Such a study has been initiated by the authors inspired by the present results.

The future role of computations in such optimizations is to address issues where experiments are limited. For example, consider the optimization of the physical shape of realistic actuators. It would be difficult to design hardware with the flexibility to provide a general shape for the actuation. But in a simulation it is straightforward to implement actuators of nearly any shape, and they may be constrained so that determined optimal geometry is realizable in hardware. This way the final configuration can be built and applied.

## References

- [1] Rechenberg, I., *Evolutionstrategie: Optimierung technischer System nach Prinzipien der biologischen Evolution*, Fromman-Holzboog, Stuttgart, 1973.
- [2] Michalewicz, Z., *Genetic Algorithms + Data Structures + Evolution Programs*, Springer-Verlag, Berlin, 1996.
- [3] Schwefel, H.-P., *Evolution and optimum seeking*, Wiley, 1995.
- [4] Freund, J. B. and Moin, P., “Jet mixing enhancement by high amplitude fluidic actuation,” *AIAA J.*, Vol. 38, No. 10, 2000.

- [5] Parekh, D. E., Kibens, V., Glezer, A., Wiltse, J. M., and Smith, D. M., "Innovative jet flow control: mixing enhancement experiments," AIAA Paper 96-0308, 1996.
- [6] Lee, M. and Reynolds, W. C., "Bifurcating and blooming jets," Report No. TF-22, Department of Mechanical Engineering, Stanford University, 1995.
- [7] Parekh, D., Leonard, A., and Reynolds, W. C., "Bifurcating jets at high Reynolds numbers," Report Nr. TF-35, Department of Mechanical Engineering, Stanford University, 1988.
- [8] Hilgers, A., *Center for Turbulence Research Annual Research Brief*, chap. Parameter optimization in jet flow control, CTR, 1999, pp. 179-194.

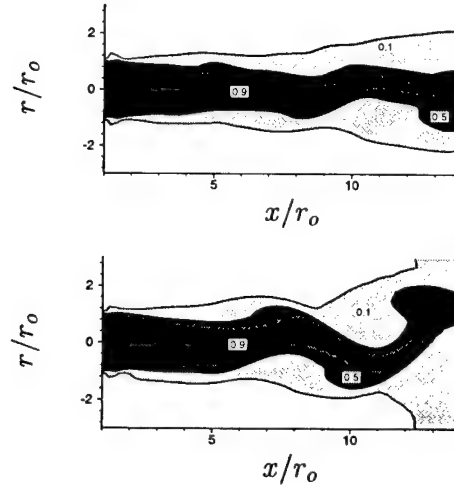


Figure 1: Jet fluid mixture fraction with the initial (top) and best (bottom) parameters.

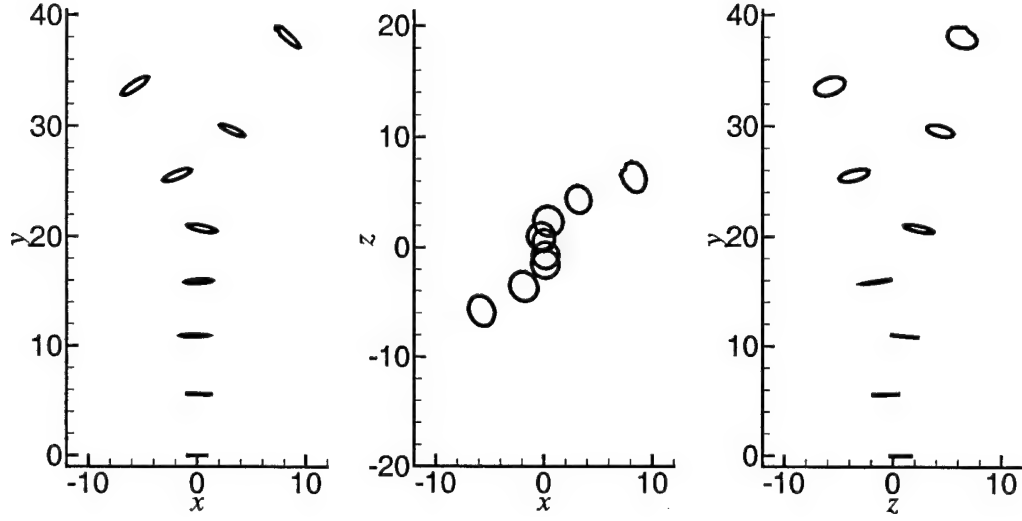


Figure 2: Vortex filament positions in the hybrid bifurcating jet with  $St_a = 0.28$ ,  $A_h = 0.63$ ,  $\beta = 2$ , and  $\phi = 0$ .

# Optimal Control of Free Shear Flow Noise

Abstract submitted for the 40<sup>th</sup> Aerospace Sciences Meeting, Reno, Jan 14-17, 2002

**M. Wei and J. B. Freund**

*Mechanical & Aerospace Engineering*

*University of California, Los Angeles*

*Los Angeles, CA 90095*

*mjwei@seas.ucla.edu*

With the advent of high-speed processors and advanced numerical methods, it has recently become possible to compute aerodynamic noise from first principles, by solving the compressible flow equations without modeling approximation.<sup>1</sup> Two-dimensional mixing layers,<sup>2</sup> axisymmetric jets,<sup>3</sup> and supersonic<sup>4</sup> and subsonic<sup>1</sup> three-dimensional turbulent jets have been computed in this way. Those simulations have provided a considerably deeper picture of the mechanisms of sound generation, but as of yet have not yielded a clear method for noise reduction. In this study we incorporate this simulation capability into a new method to analyze and control flow noise.

Our focus is jet noise and we consider a two-dimensional model of the near nozzle region. The action of an unsteady actuator is modeled by a body force acting on the shear layer near the nozzle. Our objective is to reduce radiated noise in a region of the sound field as shown schematically in figure 1 (details in the figure will be explained later). Using adjoint-based optimization,<sup>5</sup> the gradient information determined by a solution of the adjoint flow equation is used to optimize the forcing automatically.

A high order scheme with no dissipation and high resolution in wide spectrum is need to catch the sound wave accurately. Following the successful application in flow and acoustic

simulations taken by Freund<sup>4,1</sup> the sixth order Padé scheme discussed by Lele<sup>6</sup> is used in spatial differencing, and the forth order Runge-Kutta algorithm is used for time advancement. Both buffer zone<sup>7</sup> and non-reflecting boundary condition<sup>8</sup> are used to avoid the contamination from reflected wave.

The methods are benchmarked in an anti-sound problem as illustrated in Figure 2, though we stress that antisound will not be used for the mixing layer control. A noise source sits in a mean flow with Mach number 0.5. Our objective is to minimize

$$\mathcal{J} = \int_0^T \int_{\Omega} p^2 d\Omega dt,$$

where  $\Omega$  is the vertical line in Figure 2. Reducing the noise along this line is equivalent to reducing cost function  $\mathcal{J}$ . To achieve this purpose, a mass source  $\phi(\mathbf{x}, t)$  of compact support in  $C$  is optimized as

$$\phi^{k+1} = \phi^k - \alpha^k g^k,$$

where  $g$  is the gradient information from adjoint approach and  $\alpha$  is a parameter of descent which governs how large an update is made. In real calculation, this simple gradient update is inefficient because of the complexity of function  $\phi$ , So the conjugate gradient<sup>9</sup> is used for the control update, with  $\alpha$  computed at each iteration by Brent's method.<sup>9</sup> Finally, the cost  $\mathcal{J}$  is reduced by more than 95% in only 3 iterations as shown in figure 3.

As the near nozzle jet model, two-dimensional mixing layer and its radiated sound field are simulated (figure 1). The flow above(inside) the nozzle lip has Mach number 0.8, and the flow under the nozzle lip has zero velocity. Vorticity thickness  $\delta_\omega$  is used as characteristic length, and the shear speed is used as charactersitic speed. Then we choose Reynolds number 500 by definition  $Re = (u_1 - u_2)\delta_\omega/\nu$ . In this case, temperature profile is chosen

to be uniform. The small square area near the middle of left boundary is the area to put actuating force to control the acoustic field. Freund et.al's work<sup>10</sup> shows us the possibility of changing the entire jet flow structure only by actuating within near nozzle region. The line below vortices is the target area  $\Omega$  where cost function should be minimized.

The same cost function  $\mathcal{J}$  is chosen along the line to indicate the noise level. The cost is reduced by about 46% after 3 iterations (figure 4), while the maximum amplitude of the energy put to control is only about 10% of the energy of the flow. Figure 5 compares the flow and acoustic field for both the original and optimized cases at the same time. Significant sound reduction can be observed in the target area. Further improvements are expected as the method is refined and run longer.

## References

- [1] Freund, J. B., "Noise sources in a low-Reynolds-number turbulent jet at Mach 0.9," accepted *J. Fluid Mech.*, 2001.
- [2] Colonius, T., Lele, S. K., and Moin, P., "Sound generation in a mixing layer," *J. Fluid Mech.*, Vol. 330, 1997, pp. 375–409.
- [3] Mitchell, B. E., Lele, S. K., and Moin, P., "Direct computation of the sound generated by subsonic and supersonic axisymmetric jets," Tech. Rep. TF-66, Stanford University, Mechanical Engineering, November 1995.
- [4] Freund, J. B., Lele, S. K., and Moin, P., "Direct simulation of a Mach 1.92 jet and its sound field," AIAA/CEAS paper 98-2291, 1998.
- [5] Bewley, T. R., Moin, P., and Temam, R., "DNS-based predictive control of turbulence: an optimal benchmark for feedback algorithms," in preparation *J. Fluid Mech.*, 2001.

- [6] Lele, S. K., "Compact finite difference schemes with spectral-like resolution," *J. Comp. Phys.*, Vol. 103, 1992, pp. 16–42.
- [7] Freund, J. B., "A proposed inflow/outflow boundary condition for direct computation of aerodynamic sound," *AIAA J.*, Vol. 35, No. 4, 1997, pp. 740–742.
- [8] Giles, M. B., "Nonreflecting boundary conditions for Euler equations calculations," *AIAA J.*, Vol. 18, 1990, pp. 2050–2058.
- [9] Press, W., Flannery, B. P., Teukolsky, S. A., and Vetterling, W. T., 1986.
- [10] Freund, J. B. and Moin, P., "Jet mixing enhancement by high amplitude fluidic actuation," 2000.

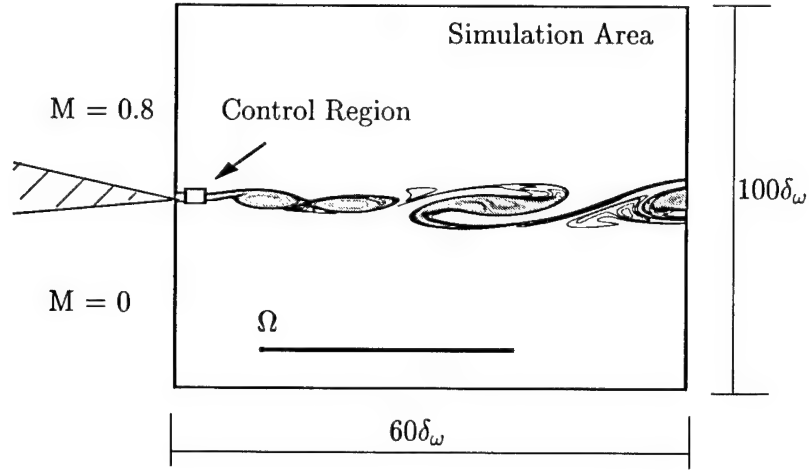


Figure 1: Mixing layer control schematic

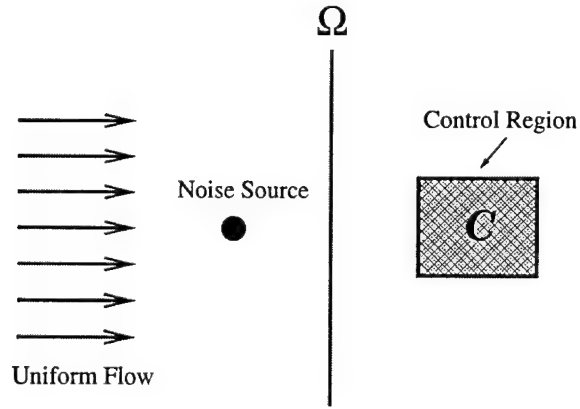


Figure 2: Anti-sound demonstration

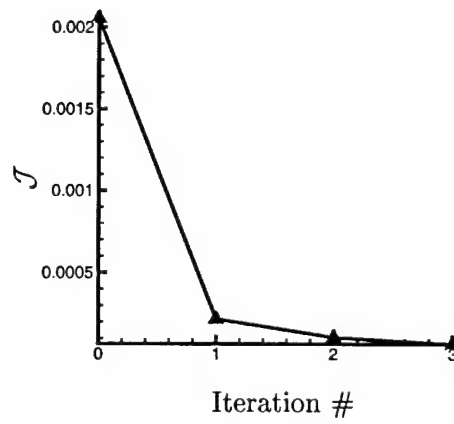


Figure 3: The reduction of cost in anti-sound problem

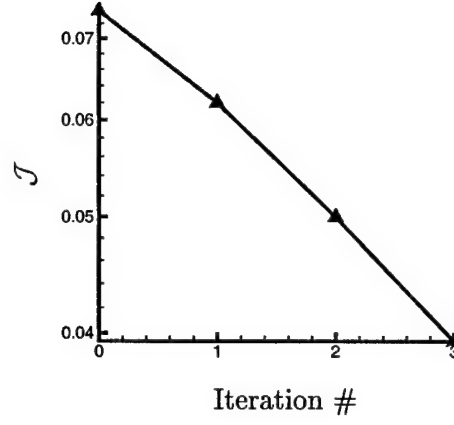


Figure 4: The reduction of cost in two-dimensional near nozzle mixing-layer

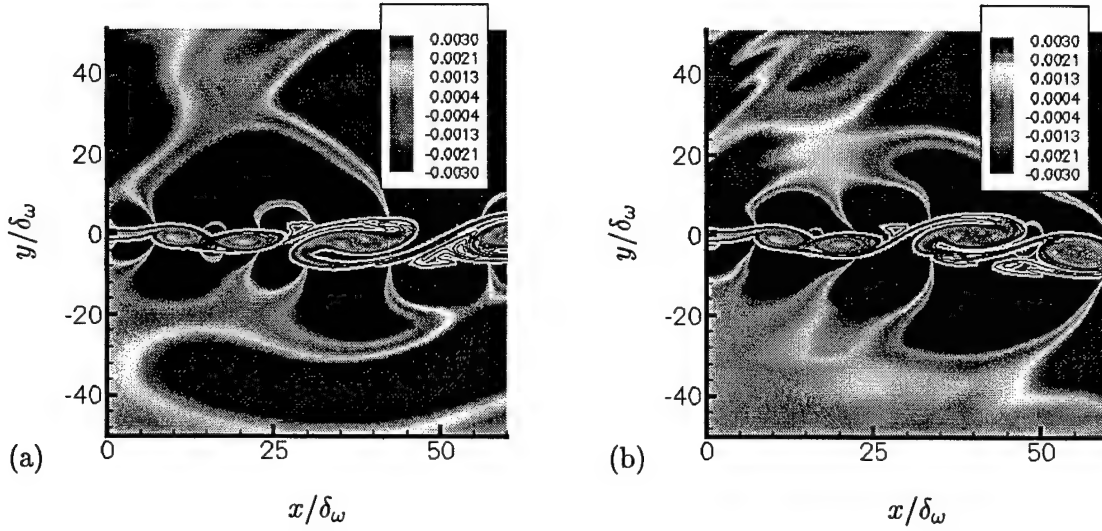


Figure 5: Comparison of (a) original and (b) optimized flow and sound field (the shade indicates sound field:  $p' = p - p_0$ ).

# Application of reduced-order controller to turbulent flows for drag reduction

Keun H. Lee, Luca Cortelezzi,<sup>a)</sup> John Kim,<sup>b)</sup> and Jason Speyer

*Department of Mechanical & Aerospace Engineering, University of California, Los Angeles, California 90095*

(Received 18 April 2000; accepted 29 January 2001)

A reduced-order linear feedback controller is designed and applied to turbulent channel flow for drag reduction. From the linearized two-dimensional Navier–Stokes equations a distributed feedback controller, which produces blowing/suction at the wall based on the measured turbulent streamwise wall-shear stress, is derived using model reduction techniques and linear-quadratic-Gaussian/loop-transfer-recovery control synthesis. The quadratic cost criterion used for synthesis is composed of the streamwise wall-shear stress, which includes the control effort of blowing/suction. This distributed two-dimensional controller developed from a linear system theory is shown to reduce the skin friction by 10% in direct numerical simulations of a low-Reynolds number turbulent nonlinear channel flow. Spanwise shear-stress variation, not captured by the distributed two-dimensional controller, is suppressed by augmentation of a simple spanwise *ad hoc* control scheme. This augmented three-dimensional controller, which requires only the turbulent streamwise velocity gradient, results in a further reduction in the skin-friction drag. It is shown that the input power requirement is significantly less than the power saved by reduced drag. Other turbulence characteristics affected by these controllers are also discussed. © 2001 American Institute of Physics. [DOI: 10.1063/1.1359420]

## I. INTRODUCTION

Much attention has been paid to the drag reduction in turbulent boundary layers. Skin friction drag constitutes approximately 50%, 90%, and 100% of the total drag on commercial aircraft, underwater vehicles, and pipelines, respectively.<sup>1</sup> The decrease of skin friction, therefore, entails a substantial saving of operational cost for commercial aircraft and submarines. Recent reviews<sup>1–3</sup> summarize achievements and open questions in boundary layer control.

With the notion that near-wall streamwise vortices are responsible for high skin friction in turbulent boundary layers, Choi *et al.*<sup>4</sup> manipulated the near-wall turbulence by applying various wall actuations. They achieved a 20% skin-friction reduction in a turbulent channel flow by applying a wall transpiration equal and opposite to the wall-normal velocity component measured at  $y^+ = 10$ . This control is shown to effectively make the streamwise vortices weaker. However, it is not easily implementable since it is difficult to place sensors inside the flow field. Other attempts at weakening the near-wall streamwise vortices have been made by imposing spanwise oscillation of the wall<sup>5</sup> and using external body force.<sup>6</sup> These methods, however, require a large amount of input energy. A reduction in skin friction must be accompanied with the required input energy much less than the energy saved by the reduction.

A systematic approach, not relying on physical intuition, has been tried in the past. A suboptimal control, which de-

termines the optimal control input by minimizing the cost functional for a short time interval, was successfully applied to the stochastic Burger's equation.<sup>7</sup> Bewley and Moin<sup>8</sup> extended the suboptimal control to a turbulent channel flow. This method, however, requires information about the whole flow field and excessive computation, so that it is impossible or at best extremely difficult to implement. It is necessary to develop a control scheme that utilizes easily measurable quantities.

Lee *et al.*<sup>9</sup> developed a neural network control algorithm that approximates the correlation between the wall-shear stresses and the wall actuation and then predicts the optimal wall actuation to produce the minimum value of skin friction. They also produced a simple control scheme from this neural network control, which determines the actuation as the sum of the weighted spanwise wall-shear stress,  $\partial w / \partial y|_w$ . Recently, Koumoutsakos<sup>10</sup> reported a substantial drag reduction obtained by applying a feedback control scheme based on the measurement and manipulation of the wall vorticity flux. Furthermore, he showed that the strength of unsteady mass transpiration actuators can be derived explicitly by inverting a system of equations.

Other systematic controls<sup>11–17</sup> have been developed by exploiting the tools recently developed in the control community.<sup>18–21</sup> Joshi *et al.*<sup>11–13</sup> and Bewley and Liu<sup>14</sup> developed an integral feedback controller, a linear quadratic (LQ) controller, and an  $\mathcal{H}_\infty$  controller (worst-case controller) to successfully stabilize unstable disturbances in transitional flow. In particular, Cortelezzi and Speyer<sup>15</sup> introduced the multi-input–multi-output (MIMO) linear-quadratic-Gaussian (LQG)/loop-transfer-recovery (LTR) synthesis,<sup>22</sup> combined with model reduction techniques, for designing an optimal linear feedback controller. This controller successfully sup-

<sup>a)</sup>Present address: Department of Mechanical Engineering, McGill University, Montreal, Quebec, Canada; electronic mail: crtiz@ametista.mecheng.mcgill.ca

<sup>b)</sup>Author to whom correspondence should be addressed. Telephone: (310) 825-4393; fax: (310) 206-4830; electronic mail: jkim@seas.ucla.edu

pressed near-wall disturbances, thus preventing a transition in two-dimensional laminar channel flows. This reduced-order controller<sup>16</sup> was applied to two-dimensional nonlinear transitional flows, illustrating that the controller designed from the linear model works remarkably well in nonlinear flows.

Our purpose in the present study is to develop a realistic robust optimal controller that systematically determines the wall actuation, in the form of blowing and suction at the wall, relying only on a measured streamwise velocity gradient to reduce skin friction in a fully developed turbulent channel flow. A dynamic representation of the flow field is required for controller design. Due to the complexity and nonlinearity of the Navier–Stokes equations, it is difficult to derive model-based controllers. Therefore, the linearized Navier–Stokes equations for Poiseuille flow are used as an approximation of the flow field and form the basis of system modeling. Several investigators (e.g., Farrel and Ioannou,<sup>23</sup> Kim and Lim,<sup>24</sup> to name a few) have shown that linearized models have a direct relevance to turbulent flows. A reduced-order controller has been designed based on this model and applied to linear and nonlinear transitional flows.<sup>15–17</sup> Encouraged by these results, in this paper we apply this distributed two-dimensional controller to a direct numerical simulation of turbulent channel flow at a low Reynolds number. We then augment our two-dimensional distributed controller by including an *ad hoc* control scheme to attenuate the residual disturbances in the spanwise direction.

In Sec. II, we derive the state-space equations from the linearized two-dimensional Navier–Stokes equations. In Sec. III, we reduce the order of the state-space equations and derive a reduced-order two-dimensional controller by using LQG/LTR synthesis. In Sec. IV, we construct and apply the distributed two-dimensional controller based on the linearized Navier–Stokes equations to a fully developed turbulent channel flow at  $Re_\tau = 100$ , where  $Re_\tau$  is the Reynolds number based on the wall-shear velocity,  $u_\tau$ , and the half-channel height,  $h$ . In Sec. V, this distributed two-dimensional controller augmented with a simple *ad hoc* control scheme is applied to the same flow. In Sec. VI, we present turbulence statistics associated with the controlled flows followed by conclusions in Sec. VII.

In this paper, we use  $(u, v, w)$  to represent the velocity components in the streamwise ( $x$ ), wall-normal ( $y$ ), and spanwise ( $z$ ) directions, respectively.

## II. THE STATE-SPACE EQUATIONS

One of the goals in the present study is to reduce the size of the controller. A controller with a large number of states is of no practical interest in engineering applications because of the amount of hardware and computer power necessary to compute a real-time control law. Consequently, it is crucial to reduce the order of the controller.

Figure 1 shows the configuration of the turbulent channel flow equipped with the controller tested for our study. Low-order controllers are usually preferred to high-order one because of the lower cost of hardware construction as well as the less computation time necessary to provide the control

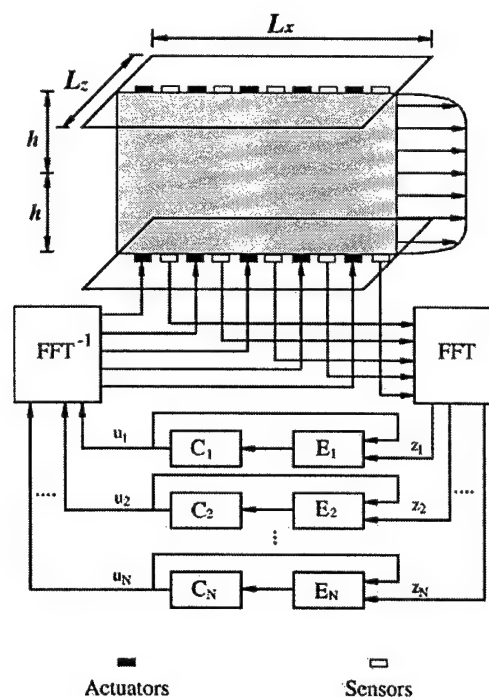


FIG. 1. Schematic representation of turbulent channel flow equipped with sensors and actuators distributed in the streamwise direction in each  $xy$  plane.

input. Hence, we slice the channel with  $xy$  planes equally spaced in the  $z$  direction in order to reduce the order of the controller. We then construct the distributed two-dimensional controller by applying the two-dimensional controller developed from the linearized two-dimensional Navier–Stokes equations<sup>15</sup> to each plane. It is shown<sup>16</sup> that the two-dimensional controller is effectively able to reduce the skin-friction drag of the finite-amplitude disturbances in a two-dimensional channel flow.

We follow the same derivation of the state-space equation as given in Cortez et al.<sup>16</sup> We give a brief outline here for completeness; the interested reader is referred to Cortez et al.<sup>16</sup> for details. The wall transpiration is applied to both top and bottom walls in a fully developed turbulent channel flow. For simplicity, though, we derive the state-space equations assuming that blowing and suction is applied only at the bottom wall. The application of blowing and suction to both walls is a trivial extension.

We consider two-dimensional incompressible Poiseuille flow in a periodic channel of streamwise length,  $L_x$ , and channel height,  $2h$ . The undisturbed velocity field has a parabolic profile with centerline velocity  $U_c$ . The linearized two-dimensional Navier–Stokes equations can be written in terms of the perturbation streamfunction,  $\psi$ ,

$$(\partial_t + U \partial_x) \Delta \psi - U'' \psi_x = Re^{-1} \Delta \Delta \psi, \quad (1)$$

where all variables are normalized with  $U_c$  and  $h$  and  $Re = U_c h / \nu$  is the Reynolds number.

To suppress perturbations evolving within the bottom boundary layer, we apply blowing and suction at the bottom wall (see Fig. 1). For simplicity, we assume that the actuators are continuously distributed. The corresponding boundary conditions are

$$\psi_x|_{y=-1} = -v_w(x, t), \quad \psi_y|_{y=\pm 1} = \psi|_{y=1} = 0, \quad (2)$$

where the control function  $v_w$  indicates blowing and suction at the bottom wall. We impose the wall transpiration of zero net mass flux.

To detect the near-wall disturbances, we measure the gradient of the streamwise disturbance velocity at given point  $x = x_i$  along the bottom wall (see Fig. 1),

$$z(x_i, t) = \psi_{yy}|_{y=-1}. \quad (3)$$

In other words, we measure the first term of the disturbance wall-shear stress,  $\tau_{yx} = \text{Re}^{-1}(\psi_{yy} - \psi_{xx})|_{y=-1}$ . The second term of the wall-shear stress is zero in the uncontrolled case and is known in the controlled case.

We define a performance index  $\tilde{J}$ , or cost criterion, to design a controller for the LQG ( $\mathcal{H}_2$ ) problem. Since we are interested in suppressing the disturbance wall-shear stress,  $\tau_{yx}$ , we define

$$\tilde{J} = \lim_{t_f \rightarrow \infty} \int_t^{t_f} \int_0^L (\psi_{yy}^2 + \psi_{xx}^2)|_{y=-1} dx dt. \quad (4)$$

The integrand represents the cost of the disturbance wall-shear stress,  $\tau_{yx}$ , being different from zero. Moreover, the integrand implicitly accounts for the cost of implementing the control itself. There are two reasons to minimize the cost of the control. In any engineering application the energy available to drive the controller is limited, and a large control action may drive the system away from the region where the linear model is valid.

By using the same procedure described in Cortezzi *et al.*,<sup>16</sup> Eqs. (1)–(3) are converted into the state-space equations:

$$\frac{dx}{dt} = \mathbf{A}\mathbf{x} + \mathbf{B}\mathbf{u}, \quad \mathbf{z} = \mathbf{C}\mathbf{x} + \mathbf{D}\mathbf{u}, \quad (5)$$

with the initial condition  $\mathbf{x}(0) = \mathbf{x}_0$ , where  $\mathbf{x}$  is the internal state vector,  $\mathbf{u}$  is the control vector,  $\mathbf{z}$  is the measurement vector. Matrices  $\mathbf{A}, \mathbf{B}, \mathbf{C}$  contain the dynamics of the two-dimensional plane Poiseuille flow, actuators, and sensors, respectively. Matrix  $\mathbf{D}$  contains the coupling between sensors and actuators. The cost criterion, Eq. (4), becomes

$$\tilde{J} = \lim_{t_f \rightarrow \infty} \int_t^{t_f} [\mathbf{z}^T \mathbf{z} + \mathbf{u}^T \mathbf{F}^T \mathbf{F} \mathbf{u}] dt, \quad (6)$$

where the superscript  $T$  denotes a transposed quantity. The matrix  $\mathbf{F}$  is obtained by spectrally decomposing the last term in the cost criterion, Eq. (4).

The advantage of the present formulation is that the whole problem decouples with respect to the wave number when Eqs. (5) and (6) are transformed into Fourier space in the streamwise direction. All matrices in Eqs. (5) and (6) are block diagonal, which allows the above state-space system into equivalent  $N$  state-space subsystems.<sup>25</sup> For a given wave number,  $\alpha$ , the state-space subsystem equations are

$$\frac{d\mathbf{x}_\alpha}{dt} = \mathbf{A}_\alpha \mathbf{x}_\alpha + \mathbf{B}_\alpha \mathbf{u}_\alpha, \quad \mathbf{z}_\alpha = \mathbf{C}_\alpha \mathbf{x}_\alpha + \mathbf{D}_\alpha \mathbf{u}_\alpha, \quad (7)$$

with the initial condition  $\mathbf{x}_\alpha(0) = \mathbf{x}_{\alpha 0}$ . It can be shown that the cost criterion, Eq. (6), also decouples with respect to the wave number (otherwise the wave number decoupling is not possible while the system itself is decoupled), and we obtain  $N$  performance indexes. For a given wave number,  $\alpha$ , the cost criterion is defined as

$$\tilde{J}_\alpha = \lim_{t_f \rightarrow \infty} \mathcal{J}_\alpha = \lim_{t_f \rightarrow \infty} \int_t^{t_f} [\mathbf{z}_\alpha^T \mathbf{z}_\alpha + \mathbf{u}_\alpha^T \mathbf{F}_\alpha^T \mathbf{F}_\alpha \mathbf{u}_\alpha] dt. \quad (8)$$

Consequently, the design of a two-dimensional controller for the system, Eq. (5), with a specified cost criterion, Eq. (6), has been reduced to the independent design of  $N$  single-wave number controllers for the subsystems, Eq. (7), along with Eq. (8).

### III. MODEL REDUCTION AND CONTROLLER DESIGN

In this section we derive a lower-order two-dimensional controller in two steps.<sup>15</sup> First, we construct a lower-order model of Eq. (7), and subsequently, design a single-wave number controller for the reduced-order model. To obtain a lower-order model, we transform Eq. (7) into a Jordan canonical form. The matrices  $\hat{\mathbf{A}}_\alpha, \hat{\mathbf{B}}_\alpha, \hat{\mathbf{C}}_\alpha, \mathbf{D}_\alpha$  that describe the dynamics of the reduced-order model are obtained from the matrices,  $\mathbf{A}_\alpha, \mathbf{B}_\alpha, \mathbf{C}_\alpha, \mathbf{D}_\alpha$  in the Jordan canonical form by retaining rows and columns corresponding to equally well controllable and observable states. The overcaret denotes the quantities associated with the reduced-order model.

Although a rigorous mathematical framework for the design of disturbance attenuation ( $\mathcal{H}_\infty$ ) linear controllers is provided by the control synthesis theory,<sup>18,19</sup> for this study LQG ( $\mathcal{H}_2$ ) synthesis is preferred. A brief review will be given in a self-contained manner to provide the necessary governing equations for closed-loop stability analysis.<sup>20</sup>

The LQG problem for each wave number  $\alpha$  is formulated as a stochastic optimal control problem described by equations

$$\dot{\hat{\mathbf{x}}}_\alpha = \hat{\mathbf{A}}_\alpha \hat{\mathbf{x}}_\alpha + \hat{\mathbf{B}}_\alpha \mathbf{u}_\alpha + \Gamma_\alpha \mathbf{w}_\alpha, \quad (9)$$

$$\hat{\mathbf{z}}_\alpha = \hat{\mathbf{C}}_\alpha \hat{\mathbf{x}}_\alpha + \mathbf{D}_\alpha \mathbf{u}_\alpha + \mathbf{v}_\alpha, \quad (10)$$

where  $\Gamma_\alpha$  is an input matrix,  $\mathbf{w}_\alpha$  and  $\mathbf{v}_\alpha$  are both white noise processes with zero means and autocorrelation functions,

$$E[\mathbf{w}_\alpha(t) \mathbf{w}_\alpha^T(\tau)] = \mathbf{W}_\alpha \delta(t - \tau), \quad (11)$$

$$E[\mathbf{v}_\alpha(t) \mathbf{v}_\alpha^T(\tau)] = \mathbf{V}_\alpha \delta(t - \tau),$$

where  $E[\cdot]$  is the expectation operator averaging over all underlying random variables and  $\delta(t - \tau)$  is the delta function. Note that  $\mathbf{W}_\alpha$  and  $\mathbf{V}_\alpha$ , the power spectral densities, will be chosen here as design parameters to enhance system performance. An additional comment on the controller design process will be given at the end of this section.

The LQG controller is determined by finding the control action  $\mathbf{u}_\alpha(Z_t)$ , where  $Z_t = \{z(\tau); 0 \leq \tau \leq t\}$  is the measurement history, which minimizes the cost criterion,

$$J_\alpha = \lim_{t_f \rightarrow \infty} \frac{1}{t_f - t} \times E \left( \int_t^{t_f} (\tilde{\mathbf{x}}_\alpha^T \mathbf{Q}_\alpha \tilde{\mathbf{x}}_\alpha + 2\tilde{\mathbf{x}}_\alpha^T \mathbf{N}_\alpha \mathbf{u}_\alpha + \mathbf{u}_\alpha^T \mathbf{R}_\alpha \mathbf{u}_\alpha) d\tau \right), \quad (12)$$

subject to the stochastic dynamics system model equations Eqs. (10)–(11). Note that, from Eqs. (7)–(8),  $\mathbf{Q}_\alpha = \hat{\mathbf{C}}_\alpha^T \hat{\mathbf{C}}_\alpha$ ,  $\mathbf{N}_\alpha = \hat{\mathbf{C}}_\alpha^T \mathbf{D}_\alpha$ , and  $\mathbf{R}_\alpha = \mathbf{D}_\alpha^T \mathbf{D}_\alpha + \mathbf{F}_\alpha^T \mathbf{F}_\alpha$ . The division by  $(t_f - t)$  ensures that the cost criterion remains finite in the presence of uncertainties in the infinite-time problem ( $t_f \rightarrow \infty$ ). Note that Eq. (12) can include Eq. (8), where

$$J_\alpha = \lim_{t_f \rightarrow \infty} \frac{1}{t_f - t} E[J_\alpha], \quad (13)$$

and the limit in Eq. (8) is explicitly denoted in Eq. (13). Note that even though the time interval is infinite, the time response is still measured by the eigenvalues of the closed-loop system. We consider the infinite-time problem with time-invariant dynamics because the controller gains become constants.

By nesting the conditional expectation with respect to  $Z_t$  within the unconditional expectation of Eq. (13), i.e.,  $E[J_\alpha] = E[E[J_\alpha/Z_t]]$ , where  $E[\cdot/Z_t]$  denotes the expectation ( $\cdot$ ) conditioned on  $Z_t$ , the cost criterion can be written as

$$J_\alpha = \lim_{t_f \rightarrow \infty} \frac{1}{t_f - t} \times E \left( \int_t^{t_f} [\tilde{\mathbf{x}}_\alpha^T \mathbf{Q}_\alpha \tilde{\mathbf{x}}_\alpha + 2\tilde{\mathbf{x}}_\alpha^T \mathbf{N}_\alpha \mathbf{u}_\alpha + \mathbf{u}_\alpha^T \mathbf{R}_\alpha \mathbf{u}_\alpha + \text{tr}(\mathbf{P}_\alpha)] d\tau \right), \quad (14)$$

where  $\tilde{\mathbf{x}}_\alpha = E[\hat{\mathbf{x}}_\alpha/Z_t]$  is the conditional mean estimate of the state  $\hat{\mathbf{x}}$  and  $\mathbf{P}_\alpha$  is the conditional error variance. This cost criterion is now minimized subject to the estimation equations discussed below. Note that  $\mathbf{P}_\alpha$  does not depend on the control [see Eq. (18) below] and, therefore, does not enter into the optimization process.

The solution to the regulator problem<sup>20</sup> is a compensator composed of a state reconstruction process, known here as a filter (in the no-noise case it is known as an observer) in cascade with a controller (see Fig. 1, where  $E_i$  is the estimator and  $C_i$  is the controller). The state estimate (conditional mean)  $\tilde{\mathbf{x}}_\alpha$  is governed by the so-called Kalman filter as

$$\begin{aligned} \dot{\tilde{\mathbf{x}}}_\alpha &= \hat{\mathbf{A}}_\alpha \tilde{\mathbf{x}}_\alpha + \hat{\mathbf{B}}_\alpha \mathbf{u}_\alpha + \hat{\mathbf{L}}_\alpha \mathbf{v}_\alpha, \\ \mathbf{v}_\alpha &= \hat{\mathbf{z}}_\alpha - \tilde{\mathbf{z}}_\alpha = \hat{\mathbf{C}}_\alpha (\hat{\mathbf{x}}_\alpha - \tilde{\mathbf{x}}_\alpha) + \mathbf{v}_\alpha. \end{aligned} \quad (15)$$

If the reduced-order system were the actual system, then  $\mathbf{v}_\alpha$  in Eq. (15) is correct. When the actual system is considered and the filter is implemented based on the reduced-state space,  $\mathbf{z}$  rather than  $\hat{\mathbf{z}}$  is the measurement and the filter residual becomes

$$\mathbf{v}_\alpha = \mathbf{z}_\alpha - \hat{\mathbf{C}}_\alpha \tilde{\mathbf{x}}_\alpha - \mathbf{D}_\alpha \mathbf{u}_\alpha. \quad (16)$$

The Kalman gain matrix  $\hat{\mathbf{L}}_\alpha$ , constructed to trade the accuracy of the new measurements against the accuracy of the state propagated from the system dynamics, is given by

$$\hat{\mathbf{L}}_\alpha = \mathbf{P}_\alpha \hat{\mathbf{C}}_\alpha^T \mathbf{V}_\alpha^{-1}, \quad (17)$$

where  $\mathbf{P}_\alpha$  is the error variance in the statistical problem.

In the infinite-time stationary formulation, the error  $\mathbf{P}_\alpha$  is the solution to the algebraic Riccati equation (ARE),

$$\hat{\mathbf{A}}_\alpha \mathbf{P}_\alpha + \mathbf{P}_\alpha \hat{\mathbf{A}}_\alpha^T + \Gamma_\alpha \mathbf{W}_\alpha \Gamma_\alpha^T - \mathbf{P}_\alpha \hat{\mathbf{C}}_\alpha^T \mathbf{V}_\alpha^{-1} \hat{\mathbf{C}}_\alpha \mathbf{P}_\alpha = 0. \quad (18)$$

If the system is  $(\hat{\mathbf{A}}_\alpha, \hat{\mathbf{C}}_\alpha)$  observable and  $(\hat{\mathbf{A}}_\alpha, \hat{\mathbf{B}}_\alpha)$  controllable, then  $\mathbf{P}_\alpha$  is positive definite. Under these assumptions, it can be shown that the difference between the internal state  $\hat{\mathbf{x}}_\alpha$  and the estimate state  $\tilde{\mathbf{x}}_\alpha$ , i.e., the error,

$$\mathbf{e}_\alpha = \hat{\mathbf{x}}_\alpha - \tilde{\mathbf{x}}_\alpha, \quad (19)$$

goes to zero as time goes to infinity. In other words, the evolution equation,

$$\dot{\mathbf{e}}_\alpha = \mathbf{A}_f \mathbf{e}_\alpha + \hat{\mathbf{L}}_\alpha \mathbf{v}_\alpha + \Gamma_\alpha \mathbf{w}_\alpha, \quad (20)$$

is stable, i.e., all the eigenvalues of the matrix,

$$\mathbf{A}_f = \hat{\mathbf{A}}_\alpha - \hat{\mathbf{L}}_\alpha \hat{\mathbf{C}}_\alpha, \quad (21)$$

have a negative real part.

Minimizing the infinite-time cost function  $J$ , Eq. (14) subject to Eq. (15) yields the following control law:

$$\mathbf{u}_\alpha = -\hat{\mathbf{K}}_\alpha \tilde{\mathbf{x}}_\alpha, \quad (22)$$

where

$$\hat{\mathbf{K}}_\alpha = \mathbf{R}_\alpha^{-1} (\hat{\mathbf{B}}_\alpha^T \mathbf{S}_\alpha + \mathbf{N}_\alpha), \quad (23)$$

and  $\mathbf{S}_\alpha$  is the solution of the algebraic Riccati equation (ARE),

$$\hat{\mathbf{A}}_\alpha \mathbf{S}_\alpha + \mathbf{S}_\alpha \hat{\mathbf{A}}_\alpha^T + \mathbf{Q}_\alpha - (\mathbf{S}_\alpha \mathbf{B}_\alpha + \mathbf{N}_\alpha) \mathbf{R}_\alpha^{-1} (\mathbf{B}_\alpha^T \mathbf{S}_\alpha + \mathbf{N}_\alpha^T) = 0. \quad (24)$$

It should be remarked that the control gain matrix  $\hat{\mathbf{K}}_\alpha$  is determined from functions only of the known dynamics coefficients  $(\hat{\mathbf{A}}_\alpha, \hat{\mathbf{B}}_\alpha)$  and the weighting in the cost criterion  $(\mathbf{Q}_\alpha, \mathbf{R}_\alpha)$ , and not the statistic of the input  $(\mathbf{V}_\alpha, \mathbf{W}_\alpha)$ . Consequently,  $\hat{\mathbf{K}}_\alpha$  is determined from a performance index as Eq. (12), independent of the stochastic inputs. If  $(\hat{\mathbf{A}}_\alpha, \hat{\mathbf{B}}_\alpha)$  is controllable and  $(\hat{\mathbf{A}}_\alpha, \mathbf{Q}_\alpha^{1/2})$  observable, then the loop coefficient matrix,

$$\mathbf{A}_c = \hat{\mathbf{A}}_\alpha - \hat{\mathbf{K}}_\alpha \hat{\mathbf{B}}_\alpha, \quad (25)$$

is stable and  $\mathbf{S}_\alpha$  is positive definite. The controllable and observable conditions can be weakened to stabilizable and detectable.<sup>21</sup>

When we combine the estimator and the regulator together, the dynamic system composed of the controlled process and filter becomes

$$\begin{pmatrix} \dot{\mathbf{e}}_\alpha \\ \dot{\tilde{\mathbf{x}}}_\alpha \end{pmatrix} = \begin{bmatrix} \mathbf{A}_f & \mathbf{0} \\ \hat{\mathbf{L}}_\alpha \hat{\mathbf{C}}_\alpha & \mathbf{A}_c \end{bmatrix} \begin{pmatrix} \mathbf{e}_\alpha \\ \tilde{\mathbf{x}}_\alpha \end{pmatrix} + \begin{pmatrix} \hat{\mathbf{L}}_\alpha \mathbf{v}_\alpha + \Gamma_\alpha \mathbf{w}_\alpha \\ \hat{\mathbf{L}}_\alpha \mathbf{v}_\alpha \end{pmatrix}. \quad (26)$$

Note that any choice of two between  $\mathbf{e}_\alpha$ ,  $\hat{\mathbf{x}}_\alpha$ , and  $\tilde{\mathbf{x}}_\alpha$  produce the same dynamics because they are algebraically related by

Eq. (19). Under the above controllability and observability assumptions,  $A_f$  and  $A_c$  have only stable eigenvalues if optimal gains  $\hat{L}_\alpha$  and  $\hat{K}_\alpha$  of Eqs. (17) and (23) are used. If the actual linear system is used, then  $x_\alpha$  and the reduced-order state estimate  $\tilde{x}_\alpha$  are used to form the closed-loop dynamic system rather than that given in Eq. (26). The eigenvalues of the dynamical matrix now dictate the system stability and will differ from the ideal case of Eq. (26).

The parameters used in our LQG design are now addressed. Since the power spectral density is not known, for simplicity of the design we consider  $V_\alpha$  and  $W_\alpha$  to be of the form  $V_\alpha = \beta I$  and  $W_\alpha = \rho I$ , where  $\beta$  and  $\rho$  are scalar and  $I$  is an identity matrix. Only the ratio of  $\beta$  and  $\rho$  is important. Furthermore, by choosing  $\Gamma_\alpha = \hat{B}_\alpha$ , loop-transfer recovery (LTR) of the LQG controller to full-state feedback<sup>18</sup> guarantees that robust performance occurs when the process noise power spectral density goes to infinity, i.e.,  $\rho \rightarrow \infty$ , provided there exists no nonminimal-phase zero in the plant. In our case, there are no nonminimal-phase zeros and robust performance means approximately obtaining 60° of phase margin and 6 db of the gain margin. Note that the choice of  $\Gamma_\alpha = \hat{B}_\alpha$  implies that the noise is generated along the wall as is the control and could be interpreted as due to wall roughness. Furthermore, the values of  $\rho$  and  $\beta$  were determined by tuning the controller in the presence of turbulent flow. The degree of loop transfer recovery varied from controller to controller.

As described above using LQG/LTR assumes that the uncertainty is at the wall and effects the dynamics in the same way as the control. Since the system has the same controllability with respect to both the control and disturbances, state-space reduction for controller design was straightforward. This is in contrast to  $\mathcal{H}_\infty$  control used by Bewley and Liu,<sup>14</sup> where uncertainty is assumed uniformly throughout the channel. Since controllability of the disturbances is different from that of the control, model reduction may not be straightforward. Furthermore, robustness in terms of traditional measures of the gain and phase margin in control engineering are also obtained by using LQG/LTR. For these reasons LQG/LTR is used for the present study instead of the unstructured uncertainty  $\mathcal{H}_\infty$  controllers.

Figure 1 links the mathematical formulation to its computational implementation by summarizing in a block diagram the control strategy described above. The two-dimensional distributed controller can be programmed in a computer routine whose input is a matrix containing the gradients of the streamwise velocity component and whose output is a matrix containing the blowing and suction at the wall. Each column of the measurement matrices contains the gradients of the streamwise velocity component along the wall at a given spanwise location. Each column is processed in parallel by a fast Fourier transform (FFT) and converted into  $z_\alpha$ 's. Each single-wave number controller, Eqs. (9)–(10), is integrated in time by, for example, a third-order low-storage Runge–Kutta scheme. The  $u_\alpha$ 's are computed in parallel. An inverse FFT converts  $u_\alpha$ 's into the columns of the matrix containing the blowing and suction at the wall along the streamwise direction. This routine can be embedded in

any Navier–Stokes solver able to handle time-dependent boundary conditions for the control of three-dimensional channel flows.

Figure 1 also provides the basic architecture for the potential implementation of the present distributed two-dimensional controller in practical engineering applications. For instance, the gradients of the streamwise velocity component can be measured by microelectromechanical-systems (MEMS) hot-film sensors.<sup>26</sup> For each  $xy$  plane, analog-to-digital converters (A/D) and digital signal processors (DSP) convert the measured gradients into  $z_\alpha$ 's. Each single-wave number controller, Eqs. (9)–(10), is replaced by a microprocessor, and parallel computation produces  $u_\alpha$ 's. A DSP and a digital-to-analog converter (D/A) produce the actuating signal in each  $xy$  plane. A variety of actuators, such as synthetic jets, microbubble actuators, and thermal actuators, can mimic small-amplitude blowing and suction at the wall.<sup>26</sup>

Although the structure of this compensator is simplified by the parallel computation (for all spanwise directions), it does require processing of all the sensor measurements (for all streamwise directions). The controller is essentially centralized because all information is used and the actuators are activated spatially over the assumed channel. Controllers based explicitly on the spatial distribution of the control, suggested by Bamieh *et al.*,<sup>27</sup> show that there is a spatial decay rate. Our controller can be constructed to represent a discrete form of their controller and given the spatial decay rate for our configuration, i.e., the size of the channel could be chosen consistent with that decay rate. Nevertheless, our representation allows a significant decrease in on-line computation by identifying the Fourier modes and the number of states associated with those modes that best reduce turbulence as discussed in the next section.

#### IV. PERFORMANCE OF A TWO-DIMENSIONAL CONTROLLER

For the purpose of testing the performance of a controller, we performed direct numerical simulations of a turbulent channel flow at  $Re_\tau = 100$ . A spectral code was used with a computational domain of  $(4\pi, 2, 4\pi/3)$  and a grid resolution of  $(32, 65, 32)$  in the  $(x, y, z)$  directions. The numerical technique used in this study is essentially the same as that of Kim *et al.*<sup>28</sup> except that the time advancement for the nonlinear terms is a third-order Runge–Kutta (RK3) method. The second-order accurate Crank–Nicolson (CN) method is used for the linear terms.

We designed a distributed two-dimensional controller in two steps. First, we designed reduced-order controllers for two-dimensional Poiseuille flow in a periodic channel of streamwise length  $L_x = 4\pi$  at  $Re = 5000$ , which has the same mean wall-shear stress as turbulent channel flow at  $Re_\tau = 100$ . Subsequently, we fine-tuned the single-wave number reduced-order controllers in order to minimize the magnitude of the Fourier coefficients of the wall-shear stresses in turbulent channel flow at  $Re_\tau = 100$ . We used  $N = 32$  and  $M = 60$  in this linear model flow. Controllers operate at both top and bottom walls in parallel. If the two-dimensional controllers without model reduction were applied at each  $z$

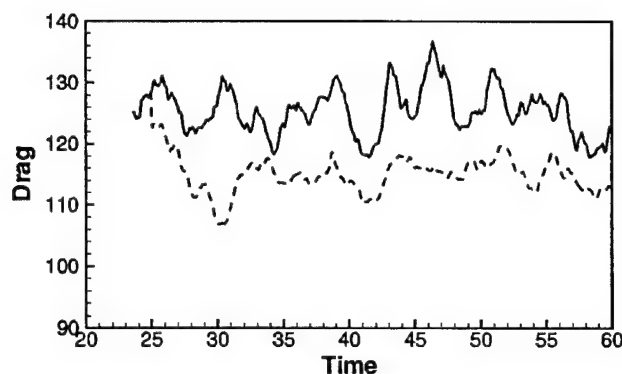


FIG. 2. Time history of the drag for the controlled and uncontrolled flows: ---, controlled flow; —, uncontrolled flow.

plane, then the order of the ensemble of controllers would be  $64 \times 3904 = 249\,856$ . Using the model reduction technique previously described, we designed eight single-wave number controllers of order 12, corresponding to the eight lowest wave numbers. Since we use the eight lowest single-wave number controllers in our simulation, the combined order of the controllers is  $64 \times 96 = 6144$ . It represents a state-space reduction of about 97.5%, with respect to the full-order system.

Figure 2 shows the time history of the drag in the uncontrolled and controlled flows. Drag is measured by the mean value of the wall-shear stresses averaged over each top and bottom wall. This two-dimensional control yields about a 10% drag reduction. Choi *et al.*<sup>4</sup> reported that the in-phase  $u$  control measured at  $y^+ = 10$  also gives a 10% drag reduction. This in-phase streamwise velocity at the wall causes a similar effect,  $du'/dy|_w \approx 0$ , which is the to-be-minimized target of our cost criterion in our two-dimensional controller. Note that this observed drag reduction is a byproduct since our controller is designed to suppress the fluctuations of the streamwise wall-shear stress, not the mean wall-shear stress. Note also the sudden drop in the drag as soon as the controller is switched on at  $t = 25$ . This transient phenomena is also observed in other studies.<sup>8,9</sup>

Figure 3 compares the magnitude of Fourier coefficients of the wall-shear stresses in the controlled and uncontrolled flows. The wall-shear stresses are measured at the bottom wall at a given spanwise location. Figures 3(a) and 3(b) show the comparisons corresponding to wave numbers  $k_x = 0.5$  and  $k_x = 1.0$ , respectively. Both figures show an order-of-magnitude reduction between the controlled and uncontrolled cases. The magnitude of the Fourier coefficients of wall-shear stress decreases very quickly as soon as the controller is activated at  $t = 25$ . These results indicate that our distributed two-dimensional linear reduced-order controller suppresses disturbance wall-shear stress remarkably well, even in a fully developed turbulent flow. The high wave number components of the wall-shear stress in Fig. 3(c) do not show any reduction since only the lowest eight single-wave number controllers (up to  $k_x = 4.0$ ) are used in the control of flow. Examinations of other spanwise locations show similar results.

Contours of the disturbance wall-shear stresses at the

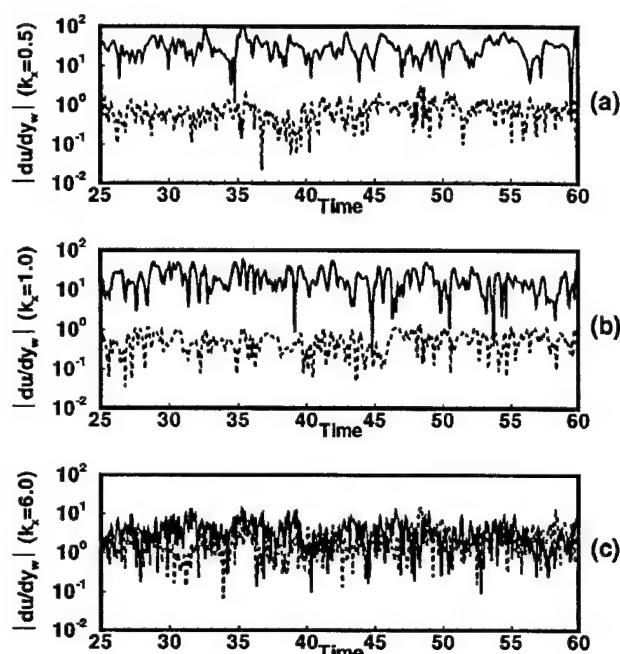


FIG. 3. Time history of the magnitude of the Fourier coefficients of the wall-shear stresses measured at the bottom wall at a given spanwise location for the controlled and uncontrolled flows: —, uncontrolled flow; ---, controlled flow. (a)  $k_x = 0.5$ , (b)  $k_x = 1.0$ , and (c)  $k_x = 6.0$ .

bottom wall in the controlled and uncontrolled flows at  $t = 30$  are shown in Fig. 4. Contours for the uncontrolled flow show the usual elongated regions of low- and high-shear stress. Note that contours for the controlled flow show the dramatic effect of the distributed two-dimensional controller. The long streaky wall-shear stress region spans almost the entire streamwise direction, indicating that the low wave number components (except the zero wave number that we do not control) are completely suppressed, which is consistent with Fig. 3. The remaining spanwise variations, i.e., the alternating regions of high- and low-shear stress, are due to

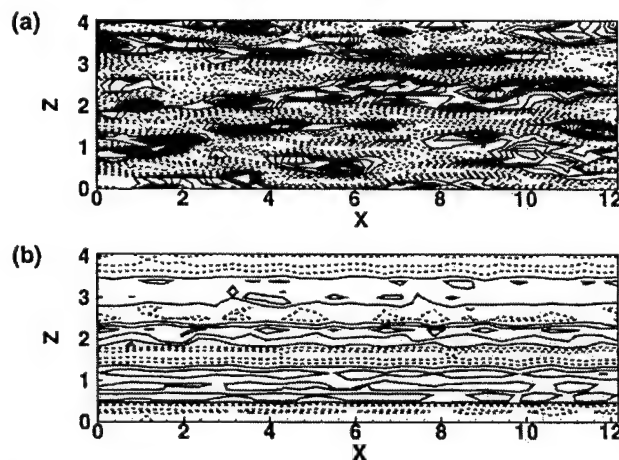


FIG. 4. Contours of disturbance wall-shear stresses at the bottom wall at  $t = 30$ : (a) uncontrolled flow; (b) 2-D-controlled flow. Negative contours are dashed.

the fact that the two-dimensional controllers distributed along the streamwise direction are operated independently from one  $z$  plane to another.

The above results demonstrate that our distributed two-dimensional controller designed from the linear model works remarkably well in suppressing near-wall disturbances in the fully developed turbulent flow. The reduction of fluctuating wall-shear stress led to drag reduction. However, this distributed two-dimensional controller has a limited impact on the total drag since it cannot control the spanwise variation of the wall-shear stress. In the next section an augmentation to the distributed two-dimensional controller is presented and implemented.

## V. AUGMENTED THREE-DIMENSIONAL CONTROLLER

In the previous section, successful control of fully developed turbulent channel flow has been obtained by applying a distributed two-dimensional controller. However, it has been observed that this controller does not account for the spanwise variations of fluid motion. An augmentation to the distributed two-dimensional controller that accommodates the three-dimensional characteristics of a fully developed turbulent flow is developed in this section.

A simple *ad hoc* control augmentation scheme is introduced in an attempt to capture the remaining spanwise variations of the controlled flow. This additional control, which generates blowing/suction to attenuate the spanwise variation of the wall-shear stress, is given as follows:

$$v_{ad}(z) = C \left( \frac{\partial u}{\partial y} \Big|_w^{(x,z)} - \frac{\partial u}{\partial y} \Big|_w^x \right), \quad (27)$$

where  $\partial u / \partial y|_w^{(x,z)}$  and  $\partial u / \partial y|_w^x$  are the streamwise velocity gradients averaged over the  $xz$  plane and the  $x$  direction, respectively, and  $C$  is a constant to be adjusted for the best performance. The subscript *ad* indicates the *ad hoc* control, and  $v_{ad}$  is a function of only  $z$ . Therefore, the new control input is defined by

$$v_w(x, z) = v_{ad} + v_{2-D}, \quad (28)$$

where  $v_{2-D}$  is the actuation velocity generated by the distributed two-dimensional controller used in the previous section.

Using the distributed two-dimensional controller augmented with this *ad hoc* control scheme, the control of the fully developed turbulent flow with  $Re_\tau = 100$  increased drag reduction to about 17%, as shown in Fig. 5. As before, the turbulent flow is left free to evolve without any wall actuation until  $t = 25$ . As soon as the controller is activated at  $t = 25$ , the drag drops sharply within a very small time period. The constant,  $C$ , in Eq. (27) is adjusted such that the root-mean-square (rms) value of the actuation is maintained at  $0.1u_\tau$ , where  $u_\tau$  is the wall-shear velocity for the uncontrolled flow. We have found empirically that  $C$  between  $0.05u_\tau$  and  $0.2u_\tau$  gives a similar performance. An introduction of this simple control augmentation enhances the drag reduction, indicating that more sophisticated controllers that best take into account the three-dimensionality of turbulent flow may produce even more efficient suppression of skin-friction drag.

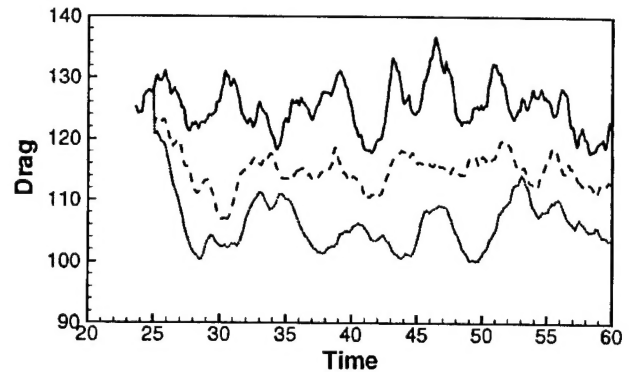


FIG. 5. Time history of the drag for the controlled and uncontrolled flows: —, uncontrolled flow; ---, 2-D-controlled flow; ···, *ad hoc*-controlled flow.

Figure 6 presents the comparison of contours of the disturbance wall-shear stresses at the bottom wall between the *ad hoc* controlled flow and the uncontrolled flow at  $t = 30$ . Compared to Fig. 4, additional effort in the spanwise direction,  $v_{ad}$ , removes the pronounced peak–valley variation of the wall-shear stress that is observed in the controlled flow with the distributed two-dimensional controllers [see Fig. 4(b)]. Note that the high wave number components of the wall-shear stress are persistently sustained because of the lowest eight single-wave number controllers adopted in the control of flow.

## VI. TURBULENCE STATISTICS

Some turbulence statistics of the flow field associated with the two controllers applied in this paper were examined to investigate the effect of the controllers on turbulence. All statistical quantities were averaged over a sufficiently long interval of time as well as over the planes parallel to the wall. For simplicity, the flows controlled by the distributed two-dimensional controller only and the distributed two-

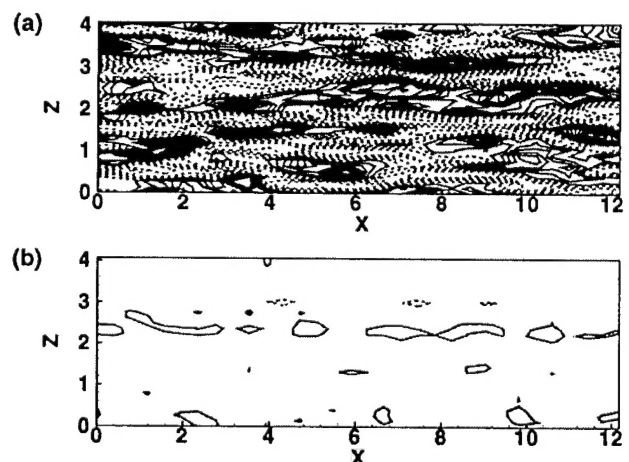


FIG. 6. Contours of disturbance wall-shear stresses at the bottom wall at  $t = 30$ : (a) uncontrolled flow; (b) *ad hoc*-controlled flow. Negative contours are dashed.

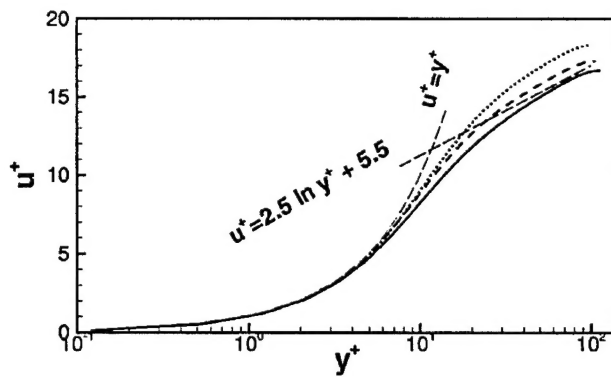


FIG. 7. Mean-velocity profiles:  $\cdots$ , *ad hoc*-controlled flow;  $---$ , 2-D-controlled flow;  $—$ , uncontrolled flow.

dimensional controller augmented with the *ad hoc* control scheme are called “2-D-controlled” and “*ad hoc*-controlled” flows, respectively.

The mean velocity profiles normalized by the actual wall-shear velocities are shown in Fig. 7 for three different channel flows. These profiles show the same trend shown in the Choi *et al.*<sup>4</sup> drag-reduced flow: the slope of the log law for controlled flows remains the same while the mean velocity itself is shifted upward in the log-law region.

The root-mean-square (rms) values of turbulent velocity fluctuations are shown in Fig. 8 and compared to those of the

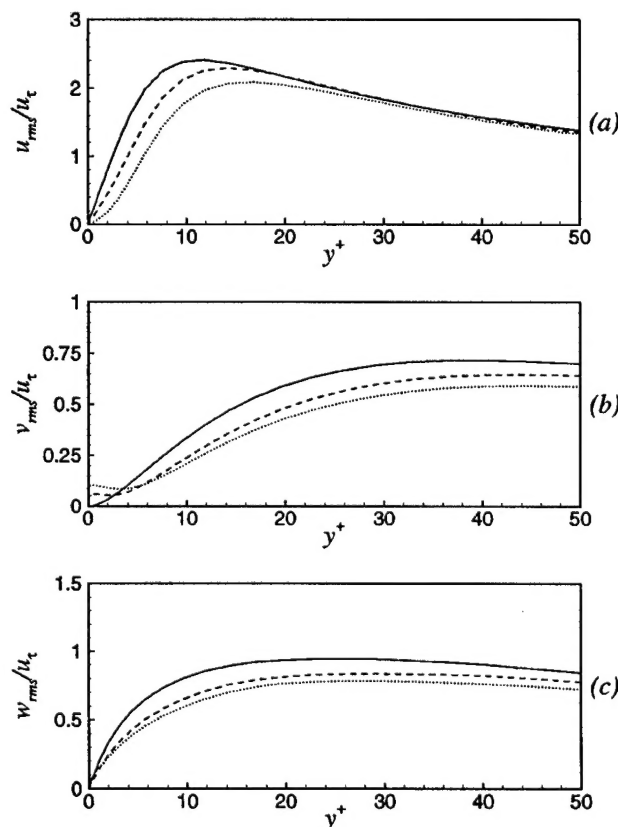


FIG. 8. Root-mean-square values of turbulent velocity fluctuations normalized by the wall-shear velocity,  $u_\tau$ , for the uncontrolled flow:  $—$ , uncontrolled flow;  $---$ , 2-D-controlled flow;  $\cdots$ , *ad hoc*-controlled flow.

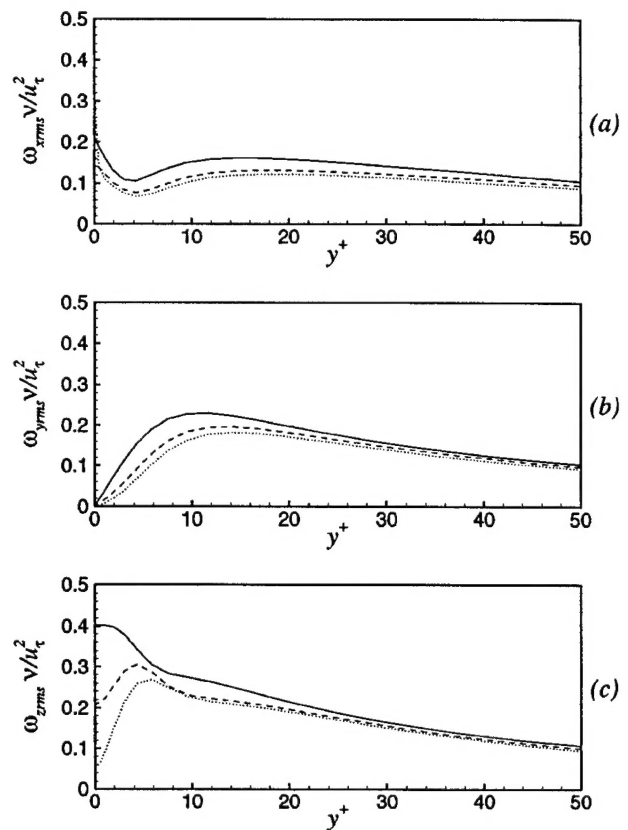


FIG. 9. Root-mean-square values of vorticity fluctuations normalized by the wall-shear velocity in wall coordinates:  $—$ , uncontrolled flow;  $---$ , 2-D-controlled flow;  $\cdots$ , *ad hoc*-controlled flow.

uncontrolled flow. Note that all quantities in this figure are normalized by the wall-shear velocity of the uncontrolled flow. The controllers reduce the value of turbulent intensity significantly throughout the channel, especially for the wall-normal and spanwise components. The reduction of these quantities in the *ad hoc*-controlled flow is greater than that in the 2-D-controlled flow. The increase in  $v_{rms}$  very near the wall is due to the control input. A similar feature is also observed by Choi *et al.*<sup>4</sup> and Lee *et al.*<sup>9</sup> Both controllers mitigate the rms of spanwise velocity fluctuation throughout the channel compared to that in uncontrolled flow. However, the introduction of  $v_{ad}$  in Eq. (27) causes this value to increase very close to the wall, which also leads to an increase in the streamwise vorticity at the wall.

Root-mean-square values of vorticity fluctuations for the controlled flows are compared with those for the uncontrolled flow in Fig. 9. All components of vorticity fluctuations are significantly reduced throughout the channel. Very close to the wall, however, the increase of streamwise vorticity in the *ad hoc*-controlled flow is due to the streamwise vorticity built at the wall by the *ad hoc* controller. The high streamwise vorticity at the wall slows the sweeping motion of high-momentum fluid induced by the streamwise vorticity away from the wall, thus resulting in a significant reduction in skin friction. A similar feature is also observed in Lee *et al.*<sup>9</sup> Note that the streamwise vorticity at the wall for the 2-D-controlled flow, however, is less than that for the uncon-

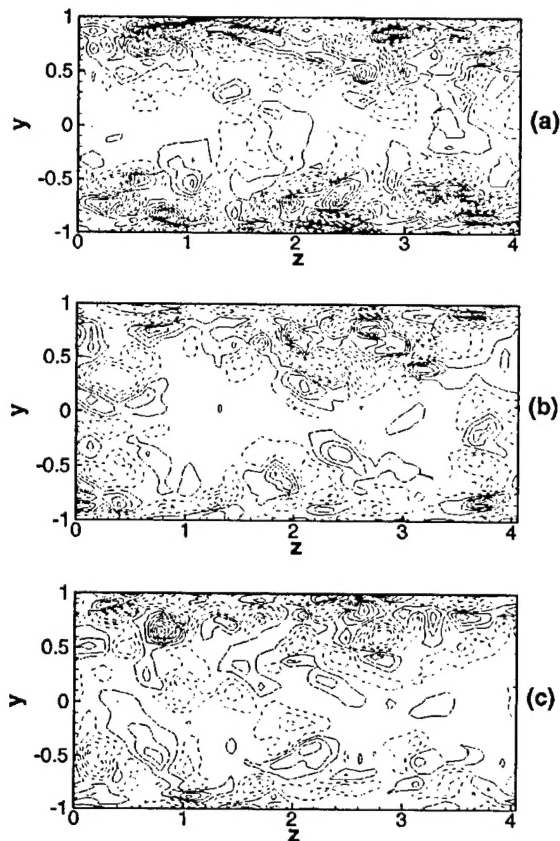


FIG. 10. A comparison of streamwise vorticity contours in a  $yz$  plane between controlled and uncontrolled flows: (a) uncontrolled flow; (b) 2-D-controlled flow; (c) *ad hoc*-controlled flow. Negative contours are dashed.

trolled flow. The reduction of  $\omega_z$  is a direct consequence of the controller, which was designed to reduce  $\partial u'/\partial y|_w$ . The reduction of  $\omega_y$  also indicates that our controllers weaken the strength of near-wall streaks. This also decreases the streak instability, which is shown to be responsible for regenerating the near-wall streamwise vortices.<sup>29,30</sup>

Figure 10 compares the streamwise vorticity fields in the uncontrolled and controlled flows. The strength of the near-wall streamwise vorticity for the controlled flows are greatly attenuated due to the wall transpiration produced by the controllers. It is discernible that the *ad hoc* controller diminishes the streamwise vorticity substantially more. The reduction of the strength of the streamwise vorticity has also been observed by Lee *et al.*<sup>9</sup> While Lee *et al.*<sup>9</sup> suppressed the streamwise vorticity field with the physical understanding that the control based on the weighted sum of  $\partial w/\partial y|_w$  can prevent the physical eruption at the wall, the present controllers attenuate the streamwise vorticity strength by minimizing the streamwise disturbance wall-shear stress systematically. The present results further support the notion that a successful attenuation of the near-wall streamwise vortices results in a significant reduction in skin-friction drag.<sup>4</sup>

## VII. CONCLUSIONS

A reduced-order linear feedback control based on a distributed two-dimensional controller design is applied to a

turbulent channel flow. A controller based on a reduced model of the linearized Navier–Stokes equations for a laminar Poiseuille flow was designed by using LQG ( $H_2$ )/LTR synthesis. This controller was implemented using input measurements that are the gradients of the streamwise disturbance velocity and output controls that are the blowing and suction at the wall.

First, we applied the distributed two-dimensional controller to both walls of a turbulent channel flow at  $Re_\tau = 100$ . Eight single-wave number controllers corresponding to eight lowest wave numbers, reducing the order of the controller about 2.5% of the order of the full size system, are applied to attain a skin-friction reduction of 10% with respect to the uncontrolled turbulent flow. Next, a simple *ad hoc* augmented control scheme of the distributed two-dimensional controller is introduced to capture the three-dimensionality of turbulent flow. The control of fully developed turbulent flow by the distributed two-dimensional controller augmented by the *ad hoc* control scheme produces a 17% reduction in skin-friction drag. Motivated by this result, we are currently developing controllers to more efficiently account for the three-dimensionality of turbulent flow.

It should be noted that the present controller, which is based on a reduced-order linear system, has achieved its design objective, i.e., minimization of the wall-shear stress disturbances, quite remarkably when applied to the nonlinear flow. It was anticipated that the reduction of disturbances would also lead to a substantial reduction of the mean wall-shear stress. Unfortunately, this turned out not to be the case, suggesting that some other cost functions should be explored. By comparing with our previous results,<sup>9,31</sup> it was found that the present controller is not as effective in diminishing the strength of the streamwise vortices in the buffer layer, which was the primary target for other controllers, but achieved its design goal by mainly affecting the region very close to the wall. In this regard, minimization of the total disturbance energy in the flow field<sup>32</sup> or minimization of the linear coupling term<sup>24</sup> appears to be a good candidate to be explored. Whether either of these cost criterion is indeed controllable in nonlinear flows, however, remains to be investigated.

This study is carried out at low Reynolds number. Whether our controller, based on the reduced-order linear model, would work in other turbulent flows, should be drawn from real experiments or simulations at high Reynolds number. However, we expect that it should work equally well for high Reynolds number flow since our controller, derived from LQG/LTR synthesis, recovers the robustness of LQR, whose characteristics have been partially tested over the different Reynolds number flows.<sup>33</sup>

The statistics of controlled and uncontrolled flows are compared. The mean velocity profile is shifted upward in the log region, a typical characteristic of drag-reduced flow. Velocity and vorticity fluctuations as well as Reynolds shear stress (not shown) are significantly reduced due to the blowing/suction generated by the controller. However, a major change is confined to the wall region. Instantaneous flow fields show that the distributed two-dimensional controller

attenuates and modifies the streaky structure of the boundary layer. Streaks are observed to span the entire streamwise direction with velocity variations in the spanwise direction. These variations are substantially reduced by the augmented controller.

The three-dimensional aspect of the distributed two-dimensional controller by the augmentation of the *ad hoc* control further reduced the skin-friction drag. This three-dimensional controller produces secondary streamwise vorticity at the wall, which slows the sweeping motions of high-momentum fluid induced by the streamwise vorticity away from the wall. This induced retarding of the primary streamwise vorticity leads to additional drag reduction, which was also observed in Choi et al.<sup>4</sup>

Regarding the scaling factor  $C$  in Eq. (27), we found an optimal value of  $C$  that yields the blowing/suction of  $0.1u_\tau$ . With this optimal  $C$ , the augmented controller generates wall transpiration with a rms value of about  $0.12u_\tau$ . The required power input per unit area to the system,  $p_w v_w + 0.5\rho v_w^3 \approx 0.1\rho u_\tau^3$ , is significantly less than the power saved from the drag reduction,  $\Delta C_f / C_f \tau_w U_c \approx 3.2\rho u_\tau^3$ , where  $p_w$ ,  $\rho$ ,  $C_f$ ,  $\tau_w$ , and  $U_c$  are the wall pressure, density, skin-friction coefficient, averaged wall-shear stress, and the centerline velocity, respectively.

Although the present two-dimensional controller augmented by an *ad hoc* three-dimensional controller has shown a promising result, it is apparent that we need to develop a three-dimensional controller using the same formulation presented in this paper. Extensions of LQG( $\mathcal{H}_2$ )/LTR design by using three-dimensional channel flow models are in progress.<sup>34,35</sup>

## ACKNOWLEDGMENTS

We thank Dr. S. Joshi and Professor R. T. McCloskey for the enlightening discussions during the course of this work. We also thank V. Ryder and Sungmoon Kang for their proofreading.

This work is supported by AFOSR Grant No. F49620-97-1-0276 and by NASA Grant No. NCC 2-374 Pr 41.

<sup>1</sup>M. Gad-el-Hak, "Interactive control of turbulent boundary layers—A futuristic overview," *AIAA J.* **32**, 1753 (1994).

<sup>2</sup>V. J. Modi, "Moving surface boundary-layer control: A review," *J. Fluids Struct.* **11**, 627 (1997).

<sup>3</sup>H. L. Reed, W. S. Saric, and D. Arnal, "Linear stability theory applied to boundary layers," *Annu. Rev. Fluid Mech.* **28**, 389 (1996).

<sup>4</sup>H. Choi, P. Moin, and J. Kim, "Active turbulence control for drag reduction in wall-bounded flows," *J. Fluid Mech.* **262**, 75 (1994).

<sup>5</sup>R. Akhavan, W. J. Jung, and N. Mangiavacchi, "Turbulence control in wall-bounded flows by spanwise oscillations," *Appl. Sci. Res.* **51**, 299 (1993).

<sup>6</sup>T. Berger, C. Lee, J. Kim, and J. Lim, "Turbulent boundary layer control utilizing the Lorentz force," *Phys. Fluids* **12**, 631 (2000).

<sup>7</sup>H. Choi, R. Temam, P. Moin, and J. Kim, "Feedback control for unsteady flow and its application to the stochastic Burgers equation," *J. Fluid Mech.* **253**, 509 (1993).

<sup>8</sup>T. Bewley and P. Moin, "Optimal control of turbulent channel flow," ASME Conference, ASME DE-Vol. 75, 1994.

<sup>9</sup>C. Lee, J. Kim, D. Babcock, and R. Goodman, "Application of neural networks to turbulence control for drag reduction," *Phys. Fluids* **9**, 1740 (1997).

<sup>10</sup>P. Koumoutsakos, "Vorticity flux control for a turbulent channel flow," *Phys. Fluids* **11**, 248 (1999).

<sup>11</sup>S. Joshi, J. L. Speyer, and J. Kim, *Proceedings of the 34th Conference on Decision and Control*, New Orleans, Louisiana, December 1995.

<sup>12</sup>S. Joshi, J. L. Speyer, and J. Kim, "A systems theory approach to the feedback stabilization of infinitesimal and finite-amplitude disturbances in plane Poiseuille flow," *J. Fluid Mech.* **332**, 157 (1997).

<sup>13</sup>S. Joshi, J. L. Speyer, and J. Kim, "Finite dimensional optimal control of Poiseuille flow," *J. Guid. Control Dyn.* **22**, 340 (1999).

<sup>14</sup>T. Bewley and S. Liu, "Optimal and robust control and estimation of linear paths to transition," *J. Fluid Mech.* **365**, 305 (1998).

<sup>15</sup>L. Cortelezzi and J. L. Speyer, "Robust reduced-order controller of laminar boundary layer transitions," *Phys. Rev. E* **58**, 1906 (1998).

<sup>16</sup>L. Cortelezzi, K. H. Lee, J. Kim, and J. L. Speyer, "Skin-friction drag reduction via robust reduced-order linear feedback control," *Int. J. Comput. Fluid Dyn.* **11**, 79 (1998).

<sup>17</sup>L. Cortelezzi, K. H. Lee, J. L. Speyer, and J. Kim, "Robust reduced-order control of turbulent channel flows via distributed sensors and actuators," in *Proceedings of the 37th Conference on Decision and Control*, Tampa, Florida, December 1998.

<sup>18</sup>K. Zhou, J. C. Doyle, and K. Glover, *Robust and Optimal Control* (Prentice-Hall, Englewood Cliffs, NJ, 1996).

<sup>19</sup>I. Rhee and J. L. Speyer, "A game theoretic approach to a finite time disturbance attenuation problem," *IEEE Trans. Autom. Control* **36**, 1021 (1991).

<sup>20</sup>A. E. Bryson and Y. C. Ho, *Applied Optimal Control* (Wiley, New York, 1969).

<sup>21</sup>H. Kwakernaak and R. Sivan, *Linear Optimal Control Systems* (Wiley Interscience, New York, 1972).

<sup>22</sup>J. C. Doyle and G. Stein, "Multivariable feedback design: Concepts for a classical/modern synthesis," *IEEE Trans. Autom. Control* **AC-26**, 4 (1981).

<sup>23</sup>B. F. Farrell and P. J. Ioannou, "Stochastic forcing of the linearized Navier-Stokes equations," *Phys. Fluids A* **4**, 1637 (1992).

<sup>24</sup>J. Kim and J. Lim, "A linear process in wall-bounded turbulent shear flows," *Phys. Fluids* **12**, 1740 (2000).

<sup>25</sup>A referee pointed out that the wave number decoupling of this control problem was also recognized by others. See, for example, Bewley and Liu (Ref. 14) and Bewley and Agarwal in *CTR Proceedings of the 1996 Summer Program*, Stanford University, December 1996.

<sup>26</sup>C. M. Ho and Y. C. Tai, "Microelectro-mechanical-systems (MEMS) and fluid flows," *J. Fluids Eng.* **118**, 437 (1996).

<sup>27</sup>B. Bamieh, F. Paganini, and M. A. Dahleh, "Distributed control of spatially invariant systems," to appear in *IEEE Trans. Automatic Control*.

<sup>28</sup>J. Kim, P. Moin, and R. Moser, "Turbulence statistics in fully-developed channel flow at low Reynolds number," *J. Fluid Mech.* **177**, 133 (1987).

<sup>29</sup>J. M. Hamilton, J. Kim, and F. Waleffe, "Regeneration mechanisms of near-wall turbulence structures," *J. Fluid Mech.* **287**, 317 (1995).

<sup>30</sup>W. Schoppa and F. Hussain, "A large-scale control strategy for drag reduction in turbulent boundary layers," *Phys. Fluids* **10**, 1049 (1998).

<sup>31</sup>C. Lee, J. Kim, and H. Choi, "Suboptimal control of turbulent channel flow for drag reduction," *J. Fluid Mech.* **401**, 245 (1998).

<sup>32</sup>P. Moin and T. Bewley, "Application of control theory to turbulence," *12th Australian Fluid Mechanics Conference*, Sydney, Australia, 10–15 December 1995.

<sup>33</sup>K. H. Lee, "A system theory approach to control of transitional and turbulent flows," Ph.D. dissertation, Department of Mechanical Engineering, University of California, Los Angeles, CA, September 1999.

<sup>34</sup>S. M. Kang, V. Ryder, L. Cortelezzi, and J. L. Speyer, "State-space formulation and control design for three-dimensional channel flows," *1999 American Control Conference*, San Diego, California, 2–4 June 1999.

<sup>35</sup>S. M. Kang, L. Cortelezzi, and J. L. Speyer, "Performance of a linear controller for laminar boundary layer transition in three dimensional channel flow," in *Proceedings of the 38th Conference on Decision and Control*, Phoenix, Arizona, 7–10 Dec. 1999.